materials

MDPI

Article

Study of Structural and Optical Properties of Titanate Nanotubes with Erbium under Heat Treatment in Different Atmospheres

Gelson L. C. Rodrigues [1,2], Tainara G. de Oliveira [2], Suziete B. S. Gusmão [2], Odair P. Ferreira [3], Thiago L. Vasconcelos [4], Yuset Guerra [5], Raquel Milani [6], Ramón Peña-Garcia [2,7] and Bartolomeu C. Viana [2,5,*]

1 Federal Institute of Piauí (IFPI), Parnaíba 64211-145, PI, Brazil
2 Interdisciplinary Laboratory of Advanced Materials (LIMAV), Materials Science and Engineering Graduate Program, Federal University of Piauí (UFPI), Teresina 64049-550, PI, Brazil
3 Department of Chemistry, State University of Londrina, Londrina 86050-482, PR, Brazil
4 National Institute of Metrology, Quality and Technology (Inmetro), Duque de Caxias 25250-02, RJ, Brazil
5 Department of Physics, Federal University of Piauí (UFPI), Teresina 64049-550, PI, Brazil
6 Department of Physics, Federal University of Pernambuco (UFPE), Recife 50670-901, PE, Brazil
7 Academic Unit of Cabo de Santo Agostinho, Federal Rural University of Pernambuco (UFRPE), Cabo de Santo Agostinho 50670-901, PE, Brazil
* Correspondence: bartolomeu@ufpi.edu.br

Abstract: Titanate nanotubes were synthesized and subjected to an ion exchange reaction with erbium salt aqueous solution to obtain titanate nanotubes exchanged with erbium (3+) ions. In order to evaluate the effects of the thermal treatment atmosphere on the structural and optical properties of erbium titanate nanotubes, we subjected them to heat treatment in air and argon atmospheres. For comparison, titanate nanotubes were also treated in the same conditions. A complete structural and optical characterizations of the samples was performed. The characterizations evidenced the preservation of the morphology with the presence of phases of erbium oxides decorating the surface of the nanotubes. Variations in the dimensions of the samples (diameter and interlamellar space) were promoted by the replacement of Na^+ by Er^{3+} and the thermal treatment in different atmospheres. In addition, the optical properties were investigated by UV–Vis absorption spectroscopy and photoluminescence spectroscopy. The results revealed that the band gap of the samples depends on the variation of diameter and sodium content caused by ion exchange and thermal treatment. Furthermore, the luminescence strongly depended on vacancies, evidenced mainly by the calcined erbium titanate nanotubes in argon atmosphere. The presence of these vacancies was confirmed by the determination of Urbach energy. The results suggest the use of thermal treated erbium titanate nanotubes in argon atmosphere in optoelectronics and photonics applications, such as photoluminescent devices, displays, and lasers.

Keywords: titanate nanotubes; erbium; ion exchange; thermal treatment; optical properties

check for updates

Citation: Rodrigues, G.L.C.; Oliveira, T.G.d.; Gusmão, S.B.S.; Ferreira, O.P.; Vasconcelos, T.L.; Guerra, Y.; Milani, R.; Peña-Garcia, R.; Viana, B.C. Study of Structural and Optical Properties of Titanate Nanotubes with Erbium under Heat Treatment in Different Atmospheres. *Materials* **2023**, *16*, 1842. https://doi.org/10.3390/ma16051842

Academic Editor: Cai Shen

Received: 17 January 2023
Revised: 27 January 2023
Accepted: 2 February 2023
Published: 23 February 2023

Copyright: © 2023 by the authors. Licensee MDPI, Basel, Switzerland. This article is an open access article distributed under the terms and conditions of the Creative Commons Attribution (CC BY) license (https://creativecommons.org/licenses/by/4.0/).

1. Introduction

Optoelectronic devices use electric charge to generate light, such as via light-emitting diodes (LEDs) and lasers, or use light to generate electric currents, such as via photodetectors and solar cells [1–3]. Such devices may be classified into light-sensitive devices and light-generating devices [1]. This classification depends on the physical mechanisms (photoemission, radiative recombination, stimulated emission, photoconductivity, photoelectric effect, among others) responsible for photon generation or the charge used for device operation [2]. In recent years, these devices have been rapidly developing and their efficiency has improved; however, the development of new nanomaterials with multifunctional applications, which are the basis of these devices, is still a growing need [1,3,4].

Semiconductor nanomaterials with one-dimensional structures (such as bars, wires, and tubes) have received much attention in recent years due to their unique physical and chemical properties compared to their respective extended solids. This implies potential applications on new devices [5,6]. These nanomaterials exhibit a wide range of electrical and optical properties that are heavily dependent on shape and size and enable applications in ceramics, gas, sensors, and biosensors, electrochemistry, photocatalysts, nano-piezoelectric and piezoelectric nanogenerators, electromechanical devices, electronics, photonics, and optoelectronics [5–7].

Among semiconductor oxides, titanium dioxide nanostructures (TiO_2) have been extensively investigated due to their promising physical and chemical properties, including low synthesis cost, high specific surface area, non-toxicity, chemical stability, environmental stability, high photoactivity, high bandgap energy, electronic mobility, and conductivity [7–10]. These properties can be adapted by their structural and surface properties, such as size, morphology, crystallinity, and surface functional groups [11], allowing potential applications in electronics, optoelectronics, magnetoelectronics, optics, catalysts, sensors, and energy conversion [8,12].

Titanate nanotubes (TiNTs), initially proposed by Kasuga et al. [13], stand out among the various nanostructures derived from TiO_2 [8]. These nanomaterials have interesting physicochemical properties, such as high specific surface area, tunnel-like structure with lamellar walls, low toxicity, and good ion exchange capacity [14–19]. In addition, the ion exchange capacity of TiNTs allows surface modifications via interaction with existing OH groups on its surface as well as the insertion of different ions in the interlamellar space [20]. These characteristics allow their use in different types of applications such as capacitor capacitance properties [21], heterogeneous photocatalysis [22], gas sensors [23], solar cells [24], lithium batteries [25], and antibacterial activity [26].

The ion exchange process between TiNTs and other transition metal ions, rare earth elements (RE), and others with various oxidation states, has been widely reported [10,18–20,27–31]. Due to its simplicity and high efficiency, this feature offers the opportunity to modify the optical and optoelectronic properties through the introduction and/or intercalation of different metal cations in the crystal structure and/or interlamellar space of the host material [18,30,32].

Some studies have pointed out that TiNTs and other TiO_2 derivatives are good candidates for RE ion host material in the preparation of photoluminescent materials [4,18,33–40]. The insertion of RE in TiO_2 nanostructures, including TiNTs, provides optical and luminescent properties that are characterized by sharp excitation and emission bands generated from the electronic transition between 4f levels [39–41]. RE insertion can modify bandgap energy and surface properties, improve thermal stability, and create oxygen defects and vacancies that influence the photocatalytic activity of the host material [39,40,42]. In addition, the high fluorescence decay lifetime, strong and sharp emission bands, and a wider absorption band are significant features of laser material [39].

Among several RE, Erbium has been considered one of the most promising due to its high chemical stability, high upconversion luminescence efficiency in the visible and ultraviolet regions, and electronic configuration that provides a long service life in the excited state [43–47]. The insertion of Er^{3+} ions into the host material may also extend the optical absorption to the visible region, decrease the recombination of photoinduced electron–hole pairs, and influence the temperature of the anatase–rutile phase transformation in TiO_2-based nanostructures [48–50].

In addition to the ion exchange process, thermal treatment can be used to improve the physicochemical properties of a material by promoting its crystallinity, converting it into a more crystalline phase, or reducing surface defects [51]. TiNTs thermal treatment invariably leads to crystalline TiO_2 formation with the achieved phase being determined by the temperature treatment and potentially by the original structure [51]. Moreover, the physicochemical properties of TiNTs (crystallinity, structure, stoichiometry, surface chemistry, among others) are strongly dependent on thermal treatment conditions (time, heating speed,

atmosphere, etc.) [11]. Recently, one of the topics that has been frequently discussed is the effect of the thermal treatment atmosphere on different nanostructures [52–56].

Here, we synthesized TiNTs (NaTiNTs and ErTiNTs) using the microwave-assisted alkaline hydrothermal method, subjected to thermal treatment in air and inert atmospheres. We focus on a more detailed characterization and the influence of thermal treatment atmosphere on the morphology, microstructure, and optical (electronic) properties of titanate nanotubes.

2. Materials and Methods

2.1. Preparation, Ion Exchange Reaction and Thermal Treatment of Titanate Nanotubes

Sodium titanate nanotubes (NaTiNTs) were synthesized based on the previous work [57]. In this synthesis, 3.0 g of TiO_2 anatase (99.98%, Sigma-Aldrich, Jurutaba, Brazil) was dispersed in 90 mL of NaOH aqueous solution (98%, Dinamica, Indaiatuba, Brazil) to a concentration of 10 Mol $L^{-1}$and magnetically stirred for 30 min. The solution was then dropped in a Teflon® reactor, autoclaved and subjected to microwave irradiation in an adapted house-microwave oven at 160 °C for 4 h. The obtained solid was centrifuged at 3500 rpm, washed with deionized water to pH = 10, and dried under vacuum for 24 h [57]. Then, the prepared NaTiNTs were subjected to ion exchange reaction with metal ions (Er^{3+}) at room temperature without any additional protonation process. For this, 500 mg of NaTiNTs were suspended in 500 mL at 0.01 Mol L^{-1} of an aqueous solution of [Er $(H_2O)_5$] $(NO_3)_3$ (99.9%, Sigma-Aldrich) (pH ≈ 5) followed by magnetic agitation at ambient temperature for 24 h. The solid was isolated by centrifugation at 3000 rpm and washed several times with deionized water for removal of nitrates. Afterward, samples exchanged with ions Er (ErTiNTs) were vacuum dried for 24 h. Finally, 200 mg of NaTiNTs and ErTiNTs were inserted in an alumina crucible, which was then placed into a quartz tube and taken to a tubular furnace for thermal treatment. The samples were heated with temperatures of 200, 400, 600, and 800 °C for 2 h with ramp heating of 10 °C/min, in air and inert (Ar) atmospheres.

2.2. Characterizations

Raman spectroscopy experiments were performed using a Bruker Senterra Raman Spectrometer equipped with an Olympus BX51 microscope, a charge-coupled device detector, 20X focus lens and a laser operating at 785 nm. The spectra were obtained from three accumulations of 20 s with an output laser power of 25 mW and a resolution of 4 cm^{-1} in the region between 1200 cm^{-1} and 85 cm^{-1}. X-ray powder diffraction patterns were obtained using a Shimadzu XRD 6000 diffractometer employing Cu-Kα radiation (λ = 1.54 Å). Data were collected with a scanning speed of 1°/min in a range of 5–60° (2θ). Scanning electron microscopy (SEM) and energy dispersive X-ray spectroscopy (EDS) was performed with a model FEI Quanta 250 FEG microscope with a Genesis Apollo X SSD detector from EDAX. High-resolution transmission electron microscopy (HRTEM) images and scanning transmission electron microscopy (STEM) images of ErTiNTs and ErTiNTs samples heat treated at 400 °C in argon atmosphere were acquired using a probe-corrected Titan 80–300 kV (FEI Co.) instrument working at 300 kV. STEM images were acquired with a high-angle annular dark field detector (HAADF) at a distance of 100 mm, which improves the contrast between Ti and Er. These samples were prepared by inserting an aqueous suspension of the material powder into a carbon-coated copper grid to allow water to evaporate at room temperature. The transmission electron microscope (TEM) Tecnai G2-20-FEI Supertwin 200 kV (FEI, Hillsboro, OR, USA) was used to acquire TEM images of ErTiNT samples heat treated in an argon atmosphere at 600 and 800 °C and ErTiNTs samples heat treated in an air atmosphere at 400, 600, and 800 °C. These samples were prepared by suspending the powder of the material in water and placing it on a copper grid coated with carbon. Diffuse solid-state UV–Vis reflectance spectroscopy was performed in a UV-2600 Shimadzu spectrophotometer (Shimadzu, Kyoto, Japan) in absorbance mode in the wavelength in the range of 200 to 800 nm. The energy of the optical band gap was calculated

using the Kubelka–Munk method for an indirect transition according to the relevant theoretical considerations [58]. The photoluminescence spectroscopy (PL) experiments were performed in a Horiba Jobin Yvon Fluorolog-3 spectrofluorometer equipped with double excitation and emission monochromator (FL-1039/40) (Horiba, Piscataway, NJ, USA). The emission spectra were obtained under 370 nm excitation and the excitation spectra were acquired by monitoring the emission at 430 nm. All measurements were collected at room temperature.

3. Results

3.1. Raman Spectroscopy

Figure 1 shows the Raman spectrum of NaTiNTs and ErTiNTs treated in air and argon atmospheres. NaTiNTs exhibit modes around 160, 190, 275, 446, 657, 703, and 906 cm^{-1} characteristic of titanate nanotubes [12,58]. The modes located at 160 and 190 cm^{-1} are related to Na-O-Ti stretching of the lattice [19], and the modes 275, 446, 657, and 703 cm^{-1} correspond to the framework Ti-O-Ti vibrations [59]. The mode at 275 cm^{-1} has been reported as an inherent mode of NaTiNTs, namely a Ti-O vibration affected by a nearby Na^+ ion [12]. Furthermore, the mode located at 906 cm^{-1} is related to Ti-O bonds, whose oxygen atom is not shared between TiO_6 units [19,26,57]. With increased temperature, the modes related to the TiNT structure of the NaTiNTs samples (Figure 1a,b) are preserved up to 400 °C in both atmospheres. In Figure 1a, beginning at 600 °C, NaTiNTs calcined in air atmosphere (NaTiNT_O_2) transform into the sodium hexatitanate phase ($Na_2Ti_6O_{13}$) which is characterized by a tunnel-like structure, without the presence of layers [57,60]. This transformation is attributed to the emergence of modes around 107, 167, 194, 222, 249, 275, 333, 363, 411, 455, 479, 677, 741, and 870 cm^{-1} [61,62]. We also observed low-intensity peaks around 450 and 605 cm^{-1} related to the rutile phase between 600 and 800 °C [42,57,61,63,64]. In Figure 1b, NaTiNTs treated in argon atmosphere (NaTiNT_Ar) underwent the same transformation as NaTiNT_O_2 from 600 °C; however, the peaks located at 194, 275, and 677 cm^{-1} are not observed as well as the peaks related to the rutile phase.

In ErTiNTs (Figure 1c,d), the ion exchange with Er^{3+} caused changes in the intensity and wavenumber of the modes located in 275, 657, 703, and 906 cm^{-1} [5,18,29,57,65,66]. These changes indicate that the ion exchange with Er^{3+}—and, consequently, the reduction of Na^+ content in the TiNTs structure—modifies the energy of these vibrations due to the difference in atomic mass and ionic radius of Na and Er (22.99 amu and 0.97 Å for Na^+ and 167.26 amu and 1.76 Å for Er^{3+}) [61,67–70]. With the increase in temperature, ErTiNTs behaved the same in both atmospheres, which includes the formation of the rutile phase evidenced by the mode at 444 cm^{-1} and the presence of the modes referring to the anatase phase [42,57]. Furthermore, no additional peaks related to erbium oxide are observed, indicating the absence of separate phases due to ion exchange and/or thermal treatment independent of atmosphere [45,57].

3.2. X-ray Diffraction

The X-ray diffractograms of the NaTiNTs and ErTiNTs are provided in Figure 2. The effects of curvature on TiNT structure are evidenced by broad reflections in all patterns analyzed. The asymmetric increase in the peaks in relation to bulk titanates is due to the distortion of the unit cell caused by the curvature of the TiNT structure [71,72]. In NaTiNTs, the characteristic crystallographic planes (200), (110), (211), and (020) of TiNTs are characterized by the peaks located at 2θ = 10, 24, 28, and 48°, respectively [73–75]. These peaks can be associated with the crystallographic data of the $Na_2Ti_3O_7{\cdot}nH_2O$ phase (JCPDS card n° 13-3129) [19]. During thermal treatment, NaTiNT_O_2 (Figure 2a) and NaTiNT_Ar (Figure 2b) preserve the TiNT structure up to 400 °C, as observed in Raman spectroscopy experiments. We also observe the formation of the sodium hexatitanate phase at 600 °C. This transition is complete at 800 °C, evidenced by the peaks located around 11.9; 14.1; 24.5; 25.8; 29.9; 32.2; 33.5; 35.9; 38.1; 43.4; 44.2; and 48.6° (2θ) [68,76]. We also observed the presence of peaks around 27.7 and 39.5° (2θ) referring to the rutile phase [42]. We

can also suggest that, regardless of the atmosphere, the heat treatment promotes a greater crystallinity of the samples. This statement is supported by the higher intensity of the peaks observed in relation to the background [68].

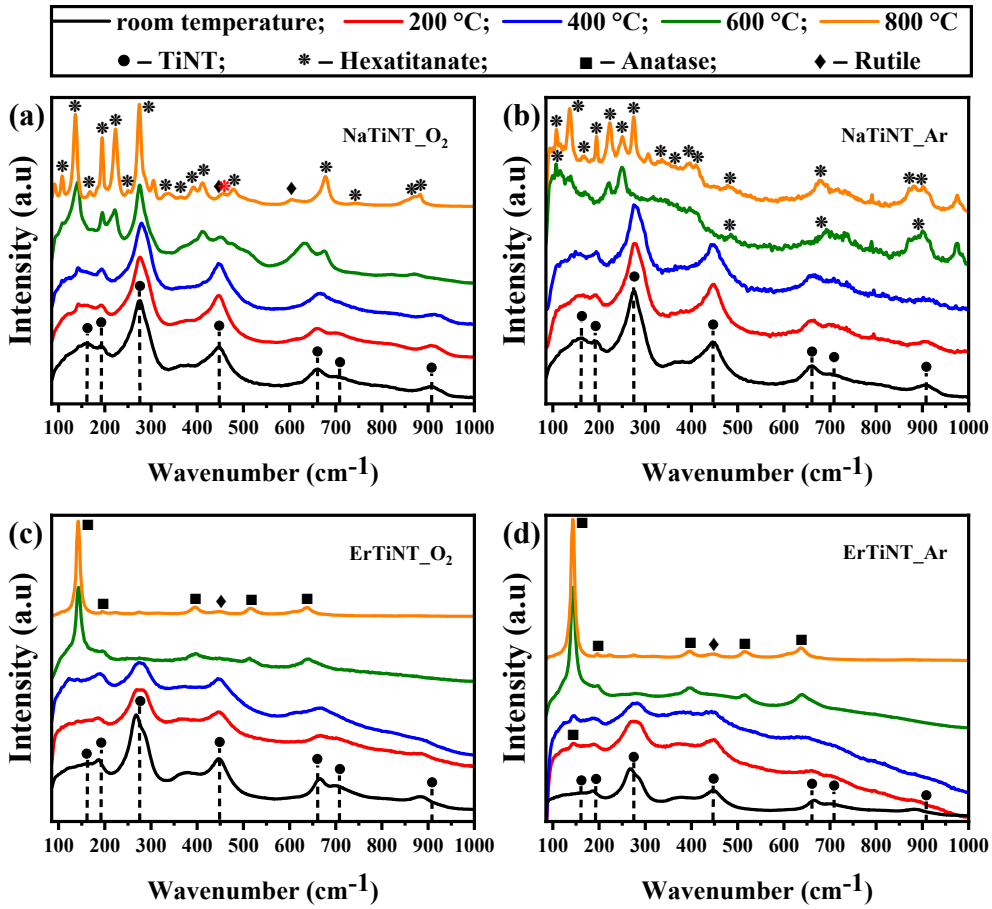


Figure 1. Raman spectra of NaTiNTs and ErTiNTs heat treated in air, (**a**) and (**c**), respectively, and argon (Ar) atmosphere, (**b**) and (**d**), respectively. The dashed lines show the characteristic peaks of the TiNTs, and the symbols indicate the phases observed during thermal treatment at different temperatures. The upper caption is the same for all samples.

The XRD profile of ErTiNTs (Figure 2c,d) indicates that both the structure and morphology of the TiNT were preserved after insertion of Er^{3+} ions into the interlamellar space. The peak located around 10° (plane (200)) related to the interlamellar distance shows a slight shift to the lower 2θ position. This displacement can be associated with an increase in the distance between the layers of the TiNT structure caused by ion exchange with Er^{3+} ions. This increase was expected due to the difference between the ionic rays (sodium less than erbium) [18]. Moreover, this change in the distance between the layers increases the curvature of the TiNT structure, causing a large distortion in the unitary cell [18,57,72]. Changes in planes 24 and 28° (2θ) (diagonal planes) may be related to the rearrangement of Er^{3+} ions in the layered titanate at different coordination positions when compared to NaTiNTs [18,65,74]. With the heat treatment, the samples of ErTiNTs in the same way that NaTiNTs maintained the TiNT structure up to 400 °C. At 600 °C, the formation of the anatase phase is evidenced by the emergence of modes around 2θ = 24.4; 37.9; 48.1; 54.0; and 55.1° [58,77]. The presence of other TiO_2 polymorphs, including TiO_2 phase (B) and rutile (27.7°), with low intensity in 800 °C [61,78], as well as the formation, in both atmospheres, of $Er_2Ti_2O_7$ (JCPDS card n°. 18-0499), is evidenced by the peak located around 31.0° [79].

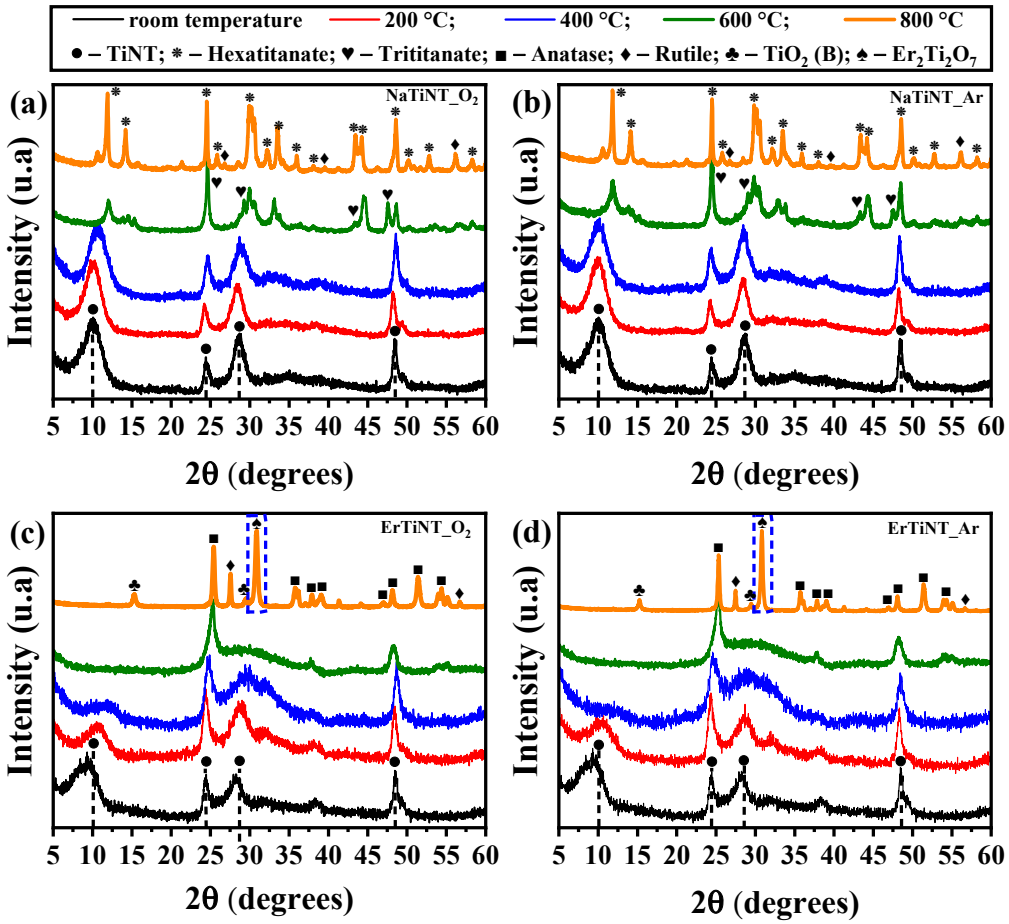


Figure 2. XRD diffractograms of NaTiNTs and ErTiNTs heat treated in air (O_2), (**a**) and (**c**), respectively, and argon atmospheres, (**b**) and (**d**), respectively. The dashed lines show the characteristic peaks of the TiNTs, and the symbols indicate the phases observed during thermal treatment at different temperatures. The dashed rectangles highlight the peak related to the erbium oxide formed. The upper caption is the same for all samples.

3.3. Morphology and Composition Analysis

The analyses performed by Raman spectroscopy and XRD indicated changes in NaTiNTs after ion exchange with Er^{3+} ions due to substitution of Na^+ by erbium ions in the interlamellar space. The chemical composition of NaTiNTs and ErTiNTs was investigated by EDS to quantify the substitution of Na^+ by erbium ions. Atomic ratios Na/Ti and Er/Ti are provided in Table 1. We can observe that the amount of Na^+ is higher in NaTiNTs compared to ErTiNTs, suggesting that the ion exchange reaction with ions Er^{3+} promotes a decrease in Na^+ allowing to observe the presence of ions Er^{3+}. We also observe the presence of residual Na^+ in the ErTiNTs. This indicates that ion exchange is efficient, but partially [57]. In addition, the thermal treatment, independent of the atmosphere, did not influence the changes in the Na/Ti or Er/Ti ratios, indicating dependence only with the ion exchange step.

Figure 3 (SEM images) illustrates fibrillar (1D) morphology of the NaTiNTs and ErTiNTs, and careful observation of the NaTiNT and ErTiNT samples reveal that TiNTs are connected in bundles [18]. From 600 °C, the heat treatment of NaTiNTs (Figure 3c,d) leads to the formation of $Na_2Ti_6O_{13}$, which presents a rod-like morphology (monoclinic phase), independent of the atmosphere [76]. The ion exchange did not alter the TiNTs fibrillar morphology of the ErTiNTs, which was maintained up to 600 °C (also independent of the atmosphere), indicating better thermal stability compared to TiNTs exchanged ionically with other RE [57]. The formation of the anatase phase at 800 °C is corroborated by the

presence of the morphology composed of nanoparticles, not nanorods (Figure 3e,f) as in the precursor sample [57].

Table 1. Samples of NaTiNT and ErTiNT heat treated in air (O_2) and argon atmospheres presenting the atomic ratios Na/Ti and Er/Ti obtained by EDS.

	Room Temperature		200 °C		400 °C		600 °C		800 °C	
Samples	**Atomic Mean of the Samples (%)**	**Ratio Na or Er/Ti (%)**	**Na/Ti**	**Er/Ti**	**Na/Ti**	**Er/Ti**	**Na/Ti**	**Er/Ti**	**Na/Ti**	**Er/Ti**
NaTiNT_O_2	8.50	0.84	0.44	-	0.75	-	0.45	-	0.63	-
NaTiNT_Ar	8.50	0.84	1.03	-	0.74	-	0.64	-	0.11	-
ErTiNT_O_2	6.20	0.30	0.27	0.12	0.0297	0.12	0.00	0.10	0.11	0.11
ErTiNT_Ar	6.20	0.30	0.14	0.11	0.09	0.10	0.00	0.11	0.16	0.11

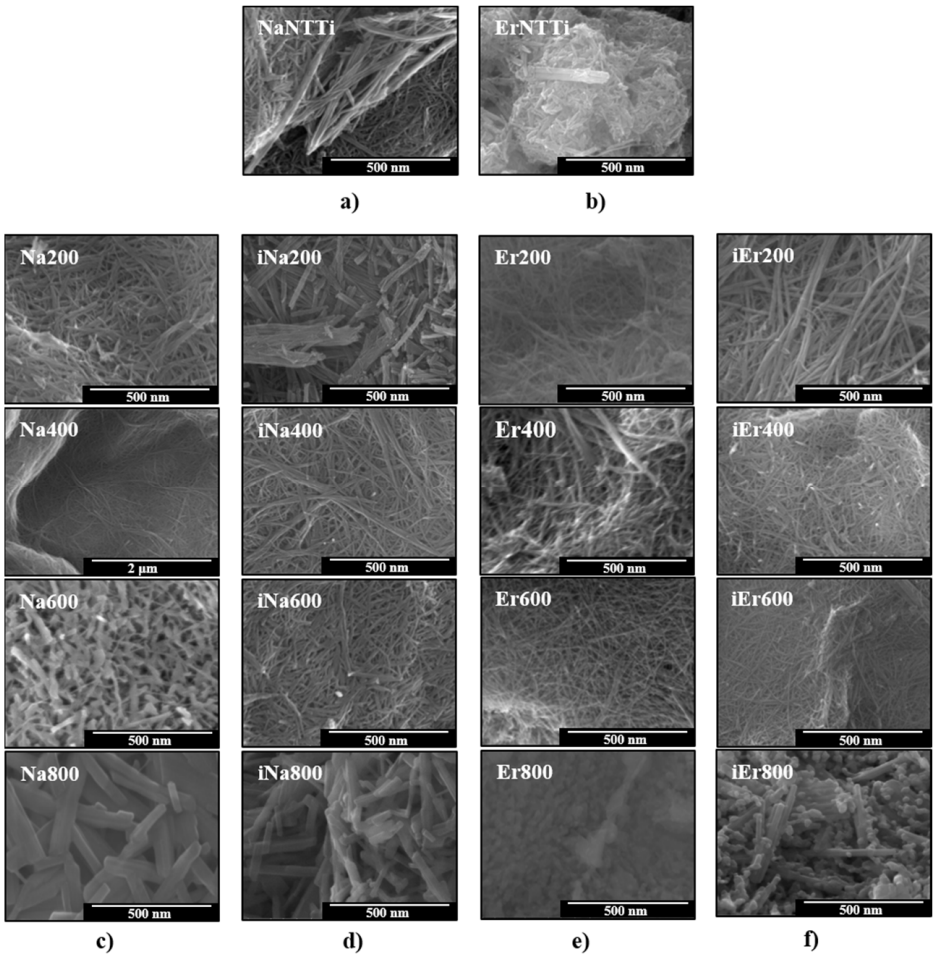


Figure 3. SEM images of (**a**) NaTiNTs and (**b**) ErTiNTs heat treated in air and argon atmosphere. In (**c**,**d**), the fibrillar morphology of NaTiNTs is preserved with increasing temperature but with a different aspect in 800 °C, indicating the probable formation of hexatitanate nanorods ($Na_2Ti_6O_{13}$). In (**e**,**f**), the fibrillar morphology of ErTiNTs is preserved up to 600 °C and clusters of NPs anatase are formed at 800 °C. The prefix "i" in columns (**d**,**f**) indicates the samples treated in inert atmosphere (argon).

Except for the analysis performed by XRD, the other techniques were not conclusive regarding the formation of nanoparticles (NPs) of erbium oxides in ErTiNTs. Thus, we performed TEM studies to confirm the results obtained by XRD. Figure 4 shows the TEM analysis of ErTiNTs at room temperature and calcined from 400 °C in air and argon atmospheres. Figure 4a illustrates that the tubular morphology of TiNTs was preserved after ion exchange, corroborating with the Raman and XRD results. This morphology was

preserved up to 400 °C and, from 600 °C, the nanotubes collapse into pieces of shorter lengths and begin to form clusters of NPs. At 800 °C, we observed the complete formation of clusters of NPs.

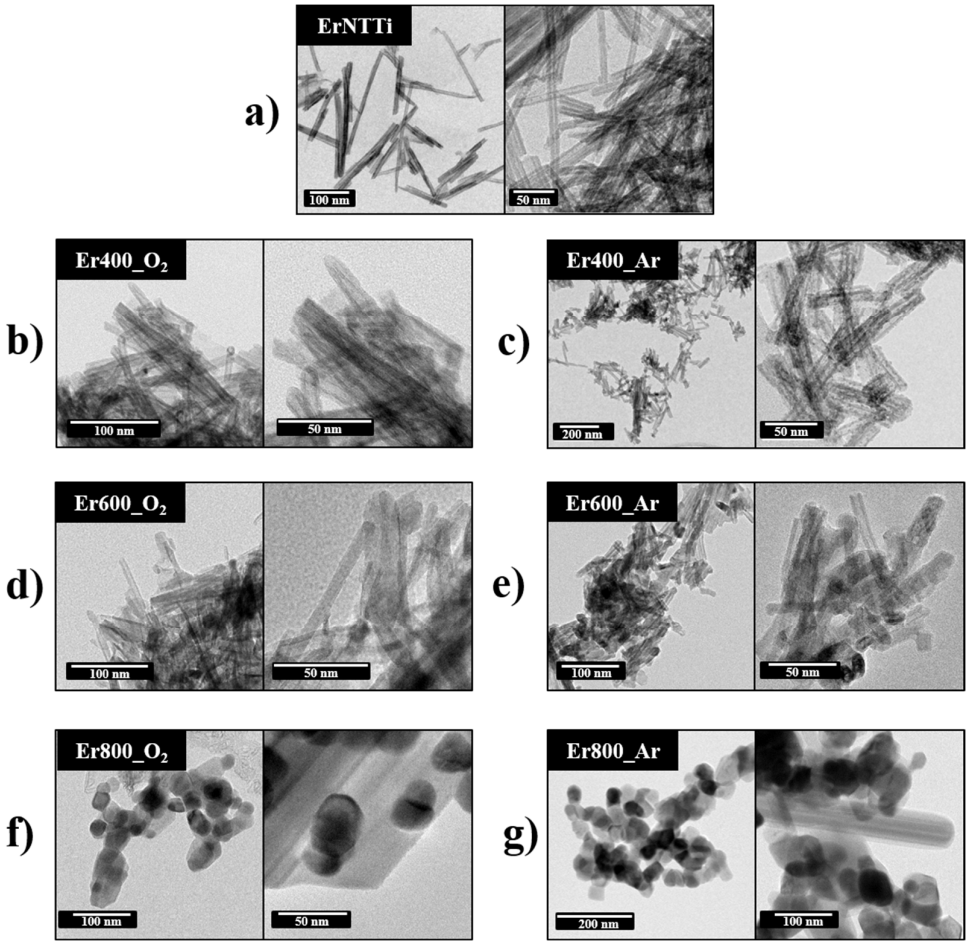


Figure 4. TEM images of ErTiNT without treatment (**a**), ErTiNT treated in air, 400 °C (**b**), 600 °C (**d**), 800 °C (**f**), and treated in Argon, 400 °C (**c**), 600 °C (**e**), 800 °C (**g**), showing the tubular morphology until 400 °C and the collapse of tubes and formation of NPs clusters of TiO_2 anatase.

Figure 5 shows the HRTEM images of the calcined ErTiNTs in air and inert atmosphere. ErTiNTs (Figure 5a–c) have an average length of 190 nm, an external diameter around 10 nm, and an average internal diameter of 4 nm. In addition, the interlamellar distance is around 0.82 nm [18]; for NaTiNTs, this measurement is around 0.70 nm in accordance with previous works [58]. These dimensions are preserved up to 400 °C in both atmospheres. However, beginning at 600 °C, we observe reductions in external (<10 nm) and internal (<3.5 nm) diameters and interlamellar distance (<0.7 nm). This behavior can be attributed to the dehydration process of the OH interlamellar group during the heat treatment, independent of the atmosphere. In addition, the clusters of NPs formed have crystalline NPs with interplanar distances around 0.33 nm, consistent with NPs of TiO_2 anatase, which agrees with previous studies [14] and corroborates the phase transition observed by Raman and XRD measurements.

In addition to TEM analyses, HAADF-STEM images of ErTiNTs show two different types of NPs (Figure 6). The first type presents very small NPs, which are probably erbium oxide clusters made of few atoms since they exhibit high Z contrast when compared to TiNTs. It is known that the contrast Z of the HAADF-STEM image is linked to the different atomic numbers of the sample atoms (22 for Ti and 68 for Er). These very small Er-based NPs are evenly distributed in TiNTs. The second type of NPs, with an average size of 5 nm,

are brighter than TiNTs but darker than NPs based on Er. These two facts suggest that these NPs are in the TiO_2 structure. Probably, TiNTs are decorated with TiO_2 NPs in the anatase phase as observed in our previously works [20,58] about the synthesis method used here. In general, the morphological and structural properties of NaTiNTs and ErTiNTs showed strong dependence on the temperature; however, dependence on the different atmospheres were not observed.

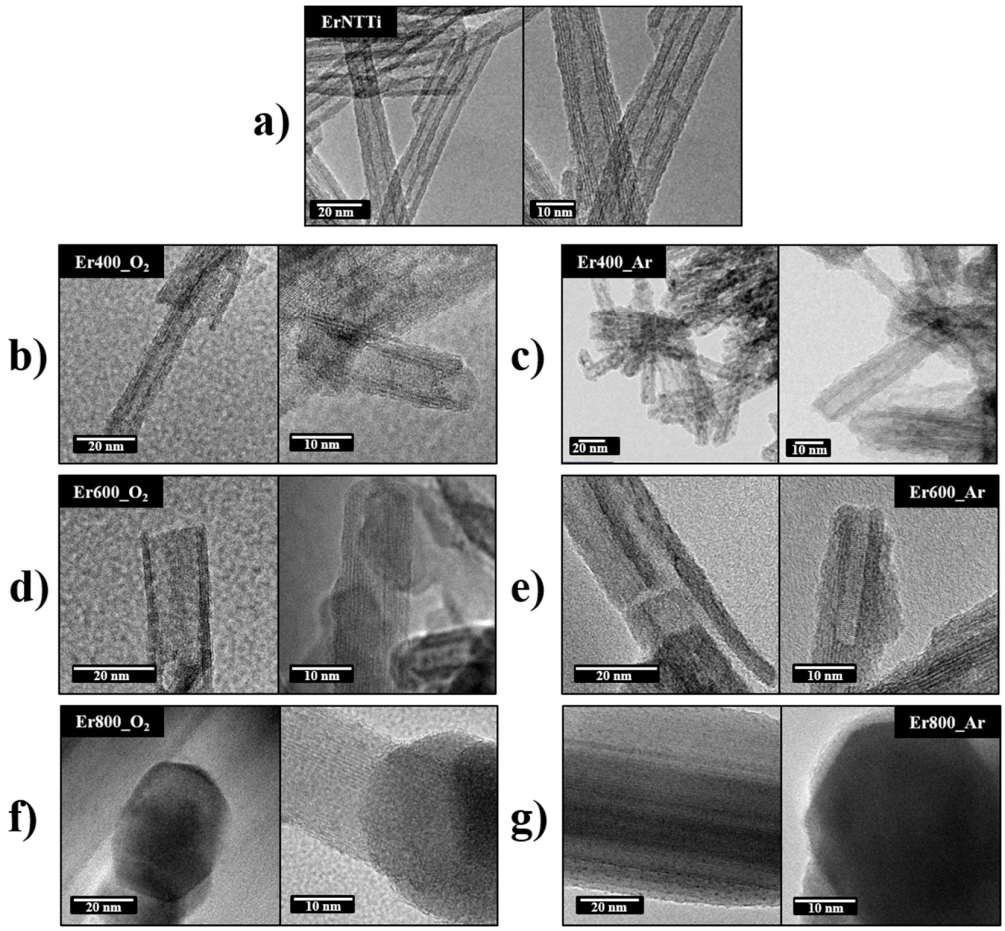


Figure 5. TEM and HAADF-STEM images of ErTNT without treatment (**a**), ErTiNT treated in air, 400 °C (**b**), 600 °C (**d**), 800 °C (**f**), and treated in Argon, 400 °C (**c**), 600 °C (**e**), 800 °C (**g**), showing Er-based NPs and NPs of TiO_2 anatase on the surface of titanate nanotubes.

3.4. Optical Properties

In order to evaluate the influence of different calcination atmosphere on the optical properties of the samples, UV–Vis absorption spectroscopy and photoluminescence (PL) experiments were performed. The UV–Visible absorption spectroscopy (solid) was performed on NaTiNTs and ErTiNTs to obtain the optical spectrum (Figure 7). We can observe that NaTiNTs have a strong absorption edge in the ultraviolet region (below 400 nm), associated with excitation of the electron O2p from the valence band to the Ti3d level of the conduction band [18,77]. With increasing temperature, NaTiNT_O_2 (Figure 7a) presented a narrow absorption edge varying between 365 and 410 nm at 800 °C [57,75,80]. NaTiNT_Ar (Figure 7b) showed a weak broad absorption range in the visible region extending to 630 nm. It is known that the electronic band gap of TiNTs depends on the tubular diameter [11]. Thus, the redshift observed in the absorption of NaTiNT_Ar may be related to the dehydration process of the OH interlamellar group, which implies contraction and, consequently, reduced diameter of the TiNT structure, less electronic band gap, and better light absorption in the visible region [11,81,82]. In addition, the dehydration process of TiNTs during thermal treatment generates oxygen vacancies that can be recombination

centers of photogenerated electrons/holes, influenced by the optical absorption of the sample [57,81]. The main difference between the optical absorptions of the samples must be in the reduction of oxygen vacancies by oxidation reactions in NaTiNT_O_2 (with a large amount of oxygen) and the maintenance of these vacancies in NaTiNT_Ar, as oxidation reactions are reduced in inert atmospheres.

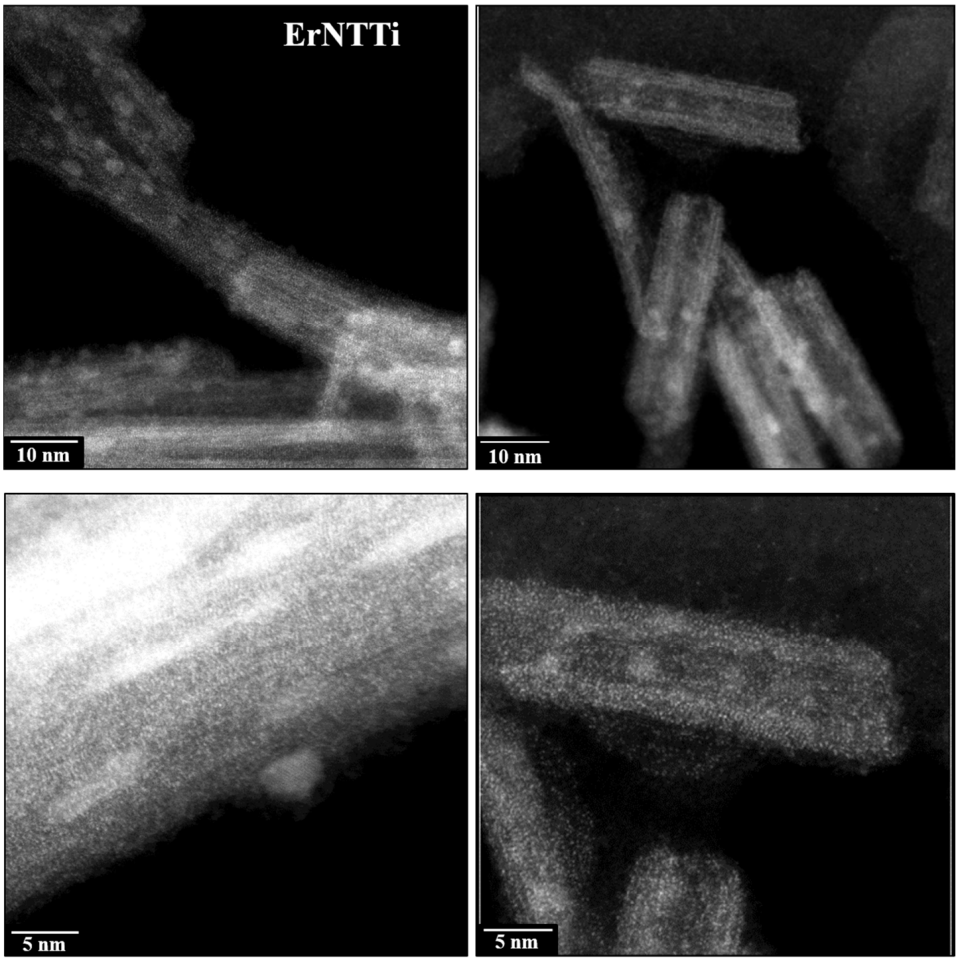


Figure 6. HAADF-STEM images of ErTiNT showing Er-based NPs and NPs of TiO_2 anatase on the surface of titanate nanotubes. The two NPS are lighter than TiNTs; however, Er-based NPs are smaller and have higher brightness.

The optical absorption spectrum of ErTiNTs presents, in addition to the absorption band in the UV region, characteristic of the TiNTs structures, a peak at 379 nm referring to the transition $^4I_{15/2} \rightarrow {}^4G_{11/2}$ of the Er^{3+} ion [83]. Peaks in the visible region are also observed around 451, 489, 524, and 655 nm and can be assigned to the transition from ground state $^2I_{15/2}$ to excited states $^4F_{3/2,5/2}$, $^4F_{7/2}$, $^2H_{11/2}$, and $^4F_{9/2}$ of the Er^{3+} ions [44,50,57,84,85]. When the temperature was increased, ErTiNT_O_2 keeps its spectral profile practically unchanged. The only changes observed are related to the peaks located at 379 nm, which reduces its intensity at 600 °C and disappears at 800 °C, and at 534 nm, which has increased intensity at 600 °C followed by a decrease at 800 °C. In addition, a redshift is observed compared to NaTiNT_O_2. Thermal treatment displaced the absorption edge of ErTiNT_O_2, which corresponds to a change in the band gap that may arise due to the phase transformations suffered by the sample [86]. The difference in the behavior of NaTiNT_O_2 and ErTiNT_O_2 spectra for the same thermal treatment atmosphere may be associated with structural dehydration caused by ion exchange and, consequently, the reduction of the amount of sodium in the sample [86,87] and the formation of different phases during thermal treatment. [57,86,87]. NaTiNTs changed to the hexatitanate phase ($Na_2Ti_6O_{13}$),

which has a higher band gap than TiO_2 anatase resulting from the transition from the TiNT phase of ErTiNTs [57,88]. The behavior of ErTiNT_Ar was similar to NaTiNT_Ar for the mechanisms that influence the improvement of optical absorption. In addition, ErTiNT_Ar display the same behavior at the peaks related to Er^{3+} ions observed in the UV and visible region of ErTiNT_O_2, which leads to synergistic effects between inert atmosphere thermal treatment and ion exchange with Er^{3+} ions, tuning the optical properties of ErTiNT_Ar compared to unmodified NaTiNTs.

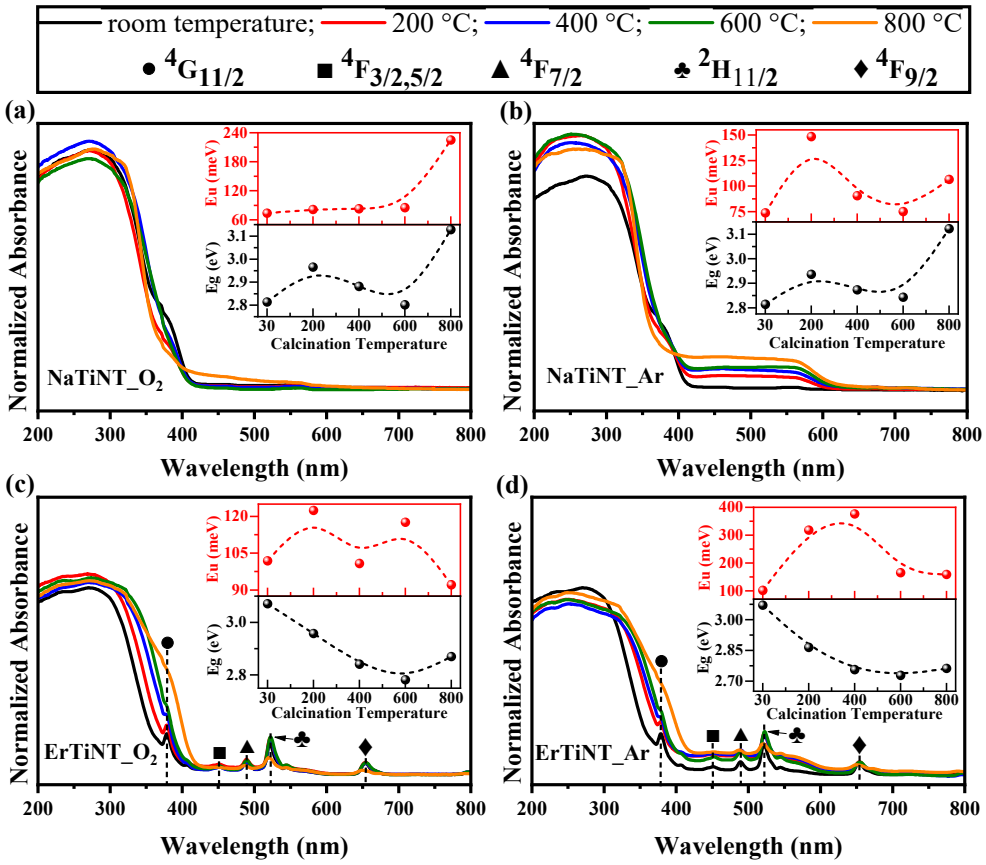


Figure 7. UV–Vis absorption spectrum of NaTiNTs heat treated in air (**a**) and Argon atmosphere (**b**), and ErTiNTs heat treated in air and argon atmospheres, (**c**) and (**d**), respectively. The dashed lines in the ErTiNTs spectra show absorption peaks that change with increasing temperature. The symbols on the absorption peaks indicate the electronic transitions from the ground state $^2I_{15/2}$. The inserts in the graphs show the band gap and Urbach energy variations of the samples with increasing temperature. The upper caption is the same for all samples.

To analyze in detail the influence of ion exchange and heat treatment on the optical absorption behavior of the samples, we estimated the band gap and Urbach energy (see insets in Figure 7 and Supplementary Figures S1–S4 in Supplementary Material) of NaTiNTs and ErTiNTs at different treatment temperatures and atmospheres. The indirect band gap of TiNT was estimated using the Tauc plot by plotting $(\alpha h\nu)^{1/2}$ versus $h\nu$ [30]. From the extrapolation of the linear part of the graph, the gap is the intersection with the energy axis $(h\nu)$. We also calculated the Urbach energy, which is associated with the absorption tail produced by the defects located inside the gap. The Urbach equation is given by $\alpha = \alpha_0 \exp(E/E_u)$, where α is the absorption coefficient, E is the photon energy, and E_u is the Urbach energy [89]. The Urbach energy is obtained by plotting $Ln\ (\alpha)$ versus E, where the value of E_u is given by the reciprocal slope of the linear portion, below the optical gap. The band gap values (E_g) for NaTiNT and ErTiNT are 2.81 eV and 3.07 eV, respectively. The E_g value obtained for the NaTiNT sample of 2.81eV is much lower than

the values reported for TiNTs, which are generally above 3 eV [19,20,90–92], shifting its absorption edge to the almost visible region. The value obtained is similar to the result reported by Bem et al. [93], who synthesized TiNTs with different sodium contents using a hydrothermal approach. Wang et al. [94] found a similar value for TiO_2 nanotubes, which was associated with the sodium content of the samples. This implies that sodium content influences the band gap of TiO_2-based materials. On the other hand, ErTiNTs presented higher band gap than NaTiNTs at room temperature. It is known that the sodium content decreased in the ionically exchange sample, which should produce lower band gap values; however, as the insertion of Er^{3+} increases the interlamellar distance and consequently the diameter of the tube, the band gap of the ErTiNTs is larger. The tubular diameter probably has greater influence than the sodium content in the band gap of TiNTs.

The band gap of NaTiNTs suffered an increase at 200 °C, followed by a decrease at 400 and 600 °C and a new increase at 800 °C. The behavior of the band gap at 200 °C was opposite to those found in the literature, where the expected value would be lower than the uncalcined sample [87,95]. This anomalous behavior can be attributed to the growth of the external diameter and reduction of the internal diameter of the TiNTs at low thermal treatment temperatures, similar to the behavior observed by Zhang et al. [96]. This increase in diameter directly influences the band gap of TiO_2-based materials [11,97]. Between 400 and 600 °C, the dehydration process of the interlamellar OH groups, controlled by the presence of sodium [87], promoted the reduction of both the interlamellar space and TiNTs diameter, reducing the band gap. The presence of sodium influenced the structural transformation of TiNT to anatase through the slower dehydration process, shifting the phase transition to higher temperatures [87,98]. Thus, NaTiNTs with $Na_2Ti_3O_7$ structure evolved to the hexatitanate phase ($Na_2Ti_6O_{13}$) at 800 °C. The basic difference between these structures is that the first presented a lamellar structure with corrugated layers of $Ti_3O_7^{2-}$ and two interlamellar Na^+ ions, while the second had a tunnel-like structure with two Na^+ ions inside the tunnel. This structure could originate from the sharing of $Ti_3O_7^{2-}$ units between adjacent $Na_2Ti_3O_7$ layers [99]. This phase has a larger band gap than TiNTs [57,88]. ErTiNTs presented a reduction in the band gap with increasing temperature up to 600 °C, followed by an increase by 800 °C due to the transition of the TiNT phase to anatase phase. However, the value of the band gap was lower than that of the NaTiNTs that changed to the hexatitanate phase as mentioned above. In addition, the values obtained for Urbach energy suggest an increase in the number of oxygen vacancies promoted by thermal treatment and ion exchange. These oxygen vacancies disturbed the band structure of the samples, promoting the observed variations of the band gaps [100].

The recombination rate of electron–hole photogenerated pairs in TiO_2-based materials is usually studied by photoluminescence spectroscopy (PL), where the PL intensity indicates the ability to stabilize photogenerated excitons [101–103]. At low-intensity, PL spectrum reflects a lower rate of recombination of the photogenerated excitons, for example [57,103]. In the case of TiO_2-based materials, PL signals are mainly due to oxygen vacancies, surface defects, and self-trapped excitons [57,104], while Er^{3+} ions have characteristic lines with narrow and sharp emission bands and a specific wavelength, originating from f-f transitions in the 4f orbital [57,105]. In Figure 8, it is possible to observe that the profiles of the PL emission spectra of NaTiNTs and ErTiNTs are similar. They have a center of band located around 425 nm. This band consists of four peaks located around 405, 421, 442, and 474 nm (Figure 9) that are originated from the recombination of the electron–hole pairs in the TNT structure after photoactivation [57,106,107]. The excitation spectra of NaTiNTs and ErTiNTs acquired by emission monitoring at 430 nm (Supplementary Figure S5 in Supplementary Material) exhibit a wide band with maximum intensity around 370 nm. This band has been attributed to titanate structures [57]. In addition, ErTiNTs have a reduction in band intensity compared to NaTiNTs and an absence of peaks characteristic of Er^{3+} ions, indicating that the emission arises from the indirect excitation of the Er^{3+} ions from the energy transfer of the excitons generated in the host TiNT. In other words, the TiNTs network absorbs the excitation energy of UV light via transition between bands. This energy is then transferred

to the Er^{3+} ions. This suggests that these ions are inserted into the spaces between the layers of the TiNT structure [45,57].

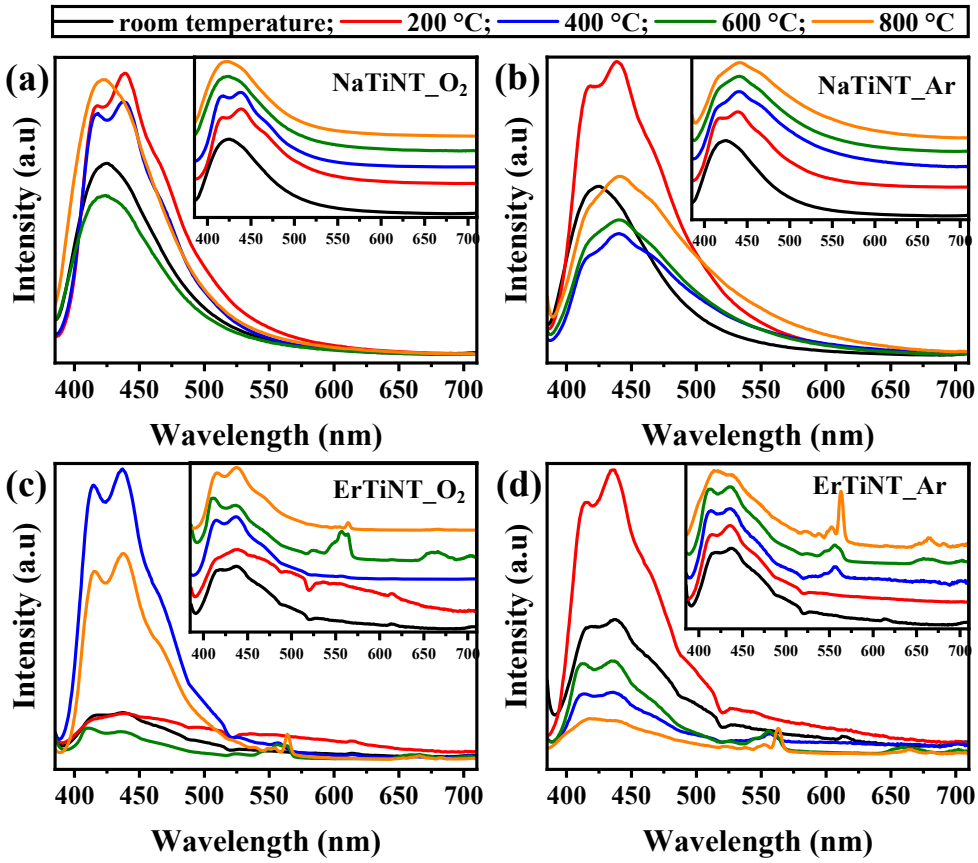


Figure 8. Emission spectra PL (excitation at 370 nm) NaTiNTs heat treated in air (**a**) and Argon atmosphere (**b**), and ErTiNTs heat treated in air and argon atmospheres, (**c**) and (**d**), respectively. Variations in PL intensity occur with increasing temperature in all samples. The insets show the spectral profile of the samples normalized and translated vertically for ease of visualization.

NaTiNT_O_2 (Figure 8a) displays an increase in intensity up to 200 °C, a decrease between 400 °C and 600 °C, and, finally, a new increase in intensity at 800 °C. This PL intensity increase at 800 °C was discussed in our previous study [57], which attributed it to the dehydration of OH groups present between the layers of the TiNT structure. This dehydration promotes the contraction and collapse of the nanotubular structure [81] and generated oxygen vacancies that can act as recombination centers for the photogenerated electron–hole pairs, resulting in a more intense PL signal [57,81]. NaTiNT_Ar (Figure 8b) had different behavior in PL intensity variations. At 200 °C, the PL intensity increased, decreasing dramatically by 400 °C, followed by further increases by 600 and 800 °C. However, the intensity at 800 °C approached the intensity of the uncalcined NaTiNTs, different from the high intensity observed in the NaTiNT_O_2 spectrum. A lower intensity of PL indicates a lower rate of recombination of the electron–hole pair and, consequently, a smaller band gap, in addition to a greater number of photogenerated carriers with longer lifetimes [30,57]. This greater separation of the electron–hole pair is improved due to the greater number of defects and vacancies [30] generated during thermal treatment in an inert atmosphere, resulting in improved photocatalytic properties and photovoltaic efficiency of the sample [57,107,108].

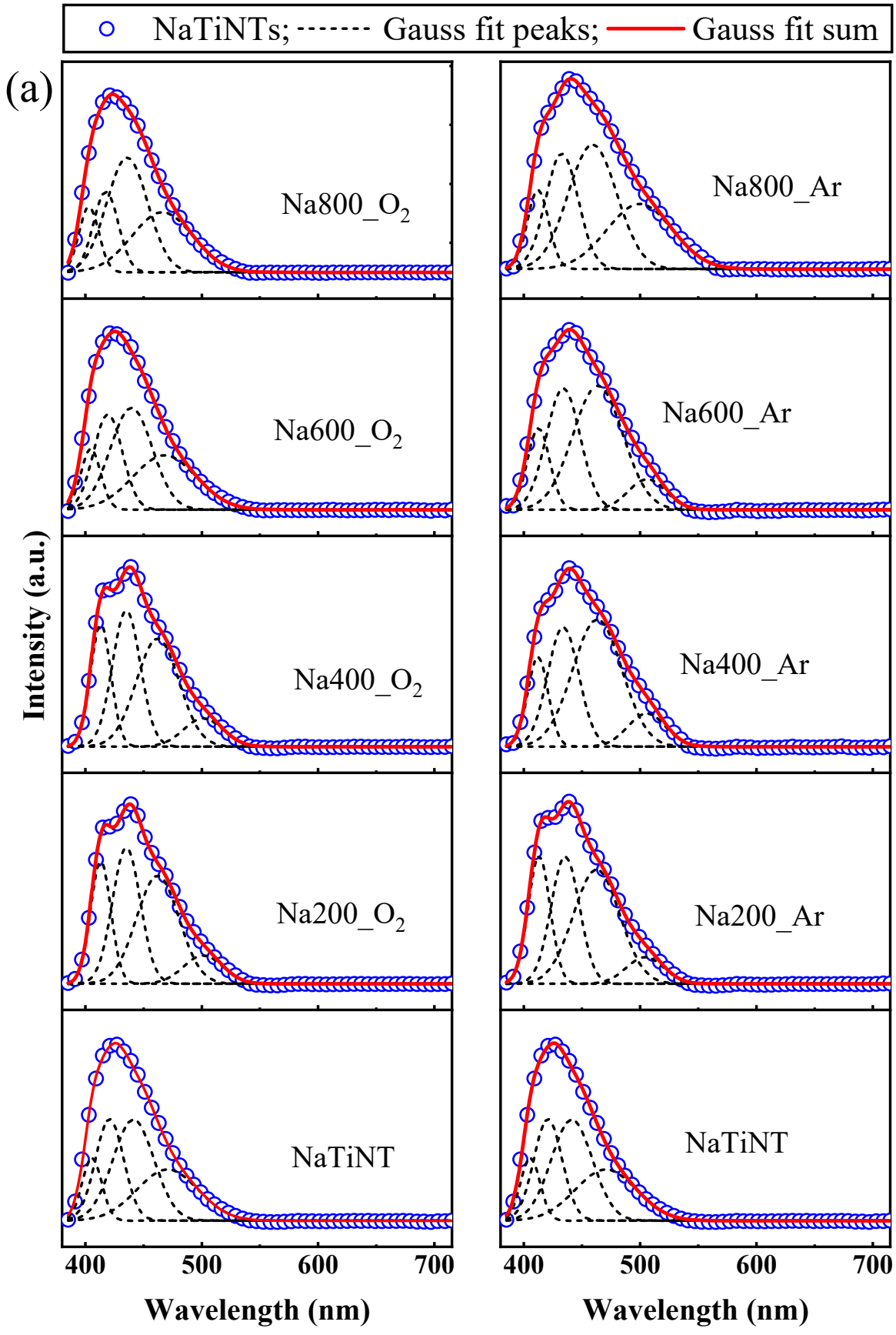


Figure 9. *Cont.*

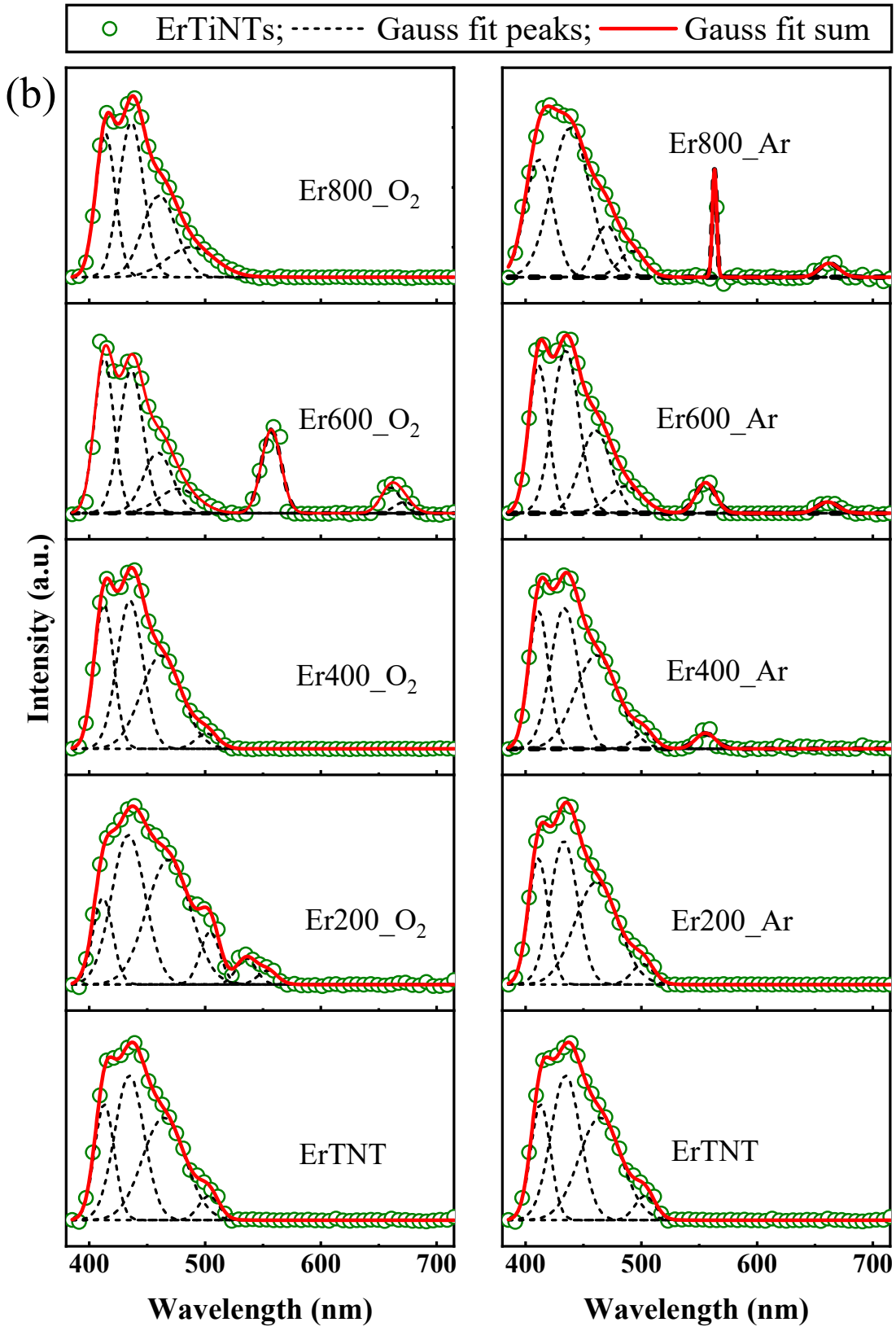


Figure 9. (**a**) Deconvolution of the PL emission spectrum (excitation at 370 nm) of NaTiNTs heat treated in air and argon atmosphere (the upper caption is the same for all samples); (**b**) deconvolution of the PL emission spectrum (excitation at 370 nm) of ErTiNTs heat treated in air and argon atmosphere (the upper caption is the same for all samples).

The PL spectrum of ErTiNT_O_2 is presented in Figure 8c, where we observed an increase in intensity up to 400 °C, followed by a decrease in 600 °C, and a new increase between 600 and 800 °C. This increased intensity by 800 °C is the result of greater recombination of the charge carriers. [57]. This higher recombination is promoted by oxygen vacancies generated by thermal treatment in the air atmosphere and by the insertion of Er^{3+} ions in host TiNT [57,109,110]. The presence of peaks located between 550 and 565 nm (visible region) refers to the transitions of the excited states ($^4S_{3/2}$) of the ground state ($^4I_{15/2}$) of the Er^{3+} ions generated from the indirect excitation of Er^{3+} ions, as discussed previously [45]. These emissions are also attributed to the strong ion–phonon interaction, where the phonon energy is small in TiO_2-based hosts, while Er^{3+} ions have higher energy due to the 4f→5d configuration implying a larger gap, making the emission of certain energy levels more probable than multi-phonon relaxation. [111]. The emergence of a peak around 665 nm at 600 °C refers to the transition $^4F_{9/2} \rightarrow {}^4I_{15/2}$ [111,112], whose intensity decreases considerably by 800 °C. This behavior has already been reported for Er^{3+} ions hosted in TiO_2-based materials, where the PL intensity of emissions in the visible spectrum first grows with increasing temperature and then decreases [112]. In Figure 8d, ErTiNT_Ar shows the growth of intensity PL at 200 °C, a reduction at 400 °C, followed by a small increase at 600 °C and a new reduction at 800 °C, which presents the lowest intensity among the thermal treatment temperatures used. These variations are similar to those observed in NaTiNT_Ar; however, with a lower intensity at 800 °C, corroborating with the previously discussed behavior. The greater separation of excitons—that is, the lower recombination rate—is improved due to the greater number of defects and vacancies generated during thermal treatment in an inert atmosphere and an increased lifetime of the photogenerated carriers' that can engage in photochemical reactions, improving the photocatalytic properties of the sample [113]. In addition, when the sample interacts with light, some well-defined energy levels are excited and then decay; however, this decay does not necessarily occur radiatively, which may explain the weaker PL intensity. This decay consists of an sequence of energy transfer of phonons from the TiNT network, combined with a low radiative energy process that ends up being seen as a PL signal [114].

An analysis of the position of the peaks in bands referring to the TiNT structure was performed with Gaussian function fitting (see Figure 9 and Figure S6 in Supplementary Material). As the peaks referring to the Er^{3+} ions did not change their positions, we will not discuss them here. With a temperature rise up to 400 °C, NaTiNT_O_2 and NaTiNT_Ar exhibited a gradual redshift that can be attributed to the thermal occupancy of the higher vibronic levels [115]. However, between 400 and 600 °C, NaTiNT_O_2 had an abrupt blueshift, which is reduced between 600 and 800 °C; while in NaTiNT_Ar, this blueshift started to reduce at 400 °C. This blueshift can be attributed to the collapse of the TiNT structure that is converted for the hexatitanate phase (nanorods), which can lead to a quantum size effect [116]. ErTiNT_O_2 and ErTiNT_Ar exhibited a redshift in PL with the insertion of Er^{3+} ions. This redshift of the band gap has been observed in previous works and can be attributed to the emission of PL by vacancies of oxygen or defects located between the bands O2p and the bands 4f of RE in NPs of RE oxides formed on the surface of nanotubular titanates, as shown by TEM images [19,31,57,117–119]. With increased temperature, ErTiNT_O_2 presented a slight blueshift while ErTiNT_Ar maintained the position of the peaks almost constantly. This behavior could be associated with the transition from the TiNT phase to the TiO_2 anatase phase in the ErTiNTs [57]. As observed, in addition to tubular diameter and sodium content, oxygen vacancies have a strong influence on the optical properties of the samples studied. Thus, the Urbach energy was calculated and we were able to confirm the presence of these vacancies, which corroborates with the UV–Vis and PL absorption results.

4. Conclusions

This study described the synthesis, structure, morphology, and optical properties of ErTiNTs (NaTiNTs ion exchanged by Er^{3+}) thermally treated in different atmospheres

with the aim of engineering the electronic properties for optoelectronic applications. We observed changes in the characteristic Raman modes of the TiNTs, an increase in the interlamellar distance of the tubular structure of the ErTiNTs, the preservation of the 1D fibrillar morphology, and an accentuated decrease in the Na/Ti ratio with the increase in the Er/Ti ratio, suggesting the effectiveness of the ion exchange process. Furthermore, variations in the dimensions of TiNTs (diameter and interlamellar space) were observed with ion exchange and different thermal treatments. The insertion of Er^{3+} ions promoted a stabilization of the anatase phase during thermal treatment. In the optical properties evaluated by UV–Vis absorption spectroscopy and PL, the samples showed changes in optical absorption and photoluminescence emission, which were related to the changes in the electronic properties promoted by insertion of Er^{3+} ions and the different phases formed during the thermal treatment. Moreover, the Urbach energy revealed the formation of oxygen vacancies that directly influence the PL emission and the band gap energy of the samples. According to the results, the insertion of Er^{3+} ions associated with thermal treatment in an inert atmosphere can tune the optoelectronics and photonics properties of titanate nanotubes. Thus, calcined ErTiNTs in argon atmosphere showed superior improvement of their optical properties in relation to the other samples analyzed, being here presented as a promising material for applications in photoluminescent devices, displays, and lasers.

Supplementary Materials: The following supporting information can be downloaded at: https://www.mdpi.com/article/10.3390/ma16051842/s1, Figure S1: The estimation of the band gap by Tauc plots of the NaTiNT_O_2 and NaTiNT_Ar samples; Figure S2: The estimation of the band gap by Tauc plots of the ErTiNT_O_2 and ErTiNT_Ar samples; Figure S3: Determination of Urbach energy of NaTiNT_O_2 and NaTiNT_Ar samples; Figure S4: Determination of Urbach energy of ErTiNT_O_2 and ErTiNT_Ar samples; Figure S5: Excitation PL spectrum (emission at 430 nm) of NaTiNTs and ErTiNTs calcined in air and argon atmosphere. The prefix "i" in figures (b) and (d) indicate the samples treated in inert atmosphere (argon). The insets were normalized and translated vertically. Variations in PL intensity occur with increasing temperature for all samples independently of the atmosphere; Figure S6: Changes (redshift and blueshift) in the positions of the peaks referent to the TiNT structure with the insertion of Er^{3+} ions and thermal treatment in air and argon atmosphere. The peaks referring to Er^{3+} ions are not presented.

Author Contributions: G.L.C.R.: formal analysis, data curation, writing—original draft, analysis and/or interpretation of data, revising the manuscript critically for important intellectual content. T.G.d.O.: acquisition of data. S.B.S.G.: formal analysis, acquisition of data, analysis and/or interpretation of data, drafting the manuscript. O.P.F.: writing—original draft, analysis and/or interpretation of data, drafting the manuscript, revising the manuscript critically for important intellectual content. T.L.V.: writing—original draft, analysis and/or interpretation of data, drafting the manuscript, revising the manuscript critically for important intellectual content. Y.G.: conceptualization, writing—original draft, data curation, formal analysis, conception and design of study, analysis and/or interpretation of data, revising the manuscript critically for important intellectual content. R.M.: acquisition of data. R.P.-G.: conceptualization, drafting the manuscript, conception, and design of study, revising the manuscript critically for important intellectual content. B.C.V.: conceptualization, funding acquisition, conception and design of study, acquisition of data, analysis and/or interpretation of data, drafting the manuscript, revising the manuscript critically for important intellectual content. All authors have read and agreed to the published version of the manuscript.

Funding: This work was supported by MCTI/CNPQ/Universal 28/2018 (Grants # 427084/2018-0), and the FAPEPI Nº 015/2017-Energia Renováveis (Grants # 001/2018-FAPEPI). Prof. B.C. Viana acknowledges the support from the produtividade em Pesquisa-PQ/CNPq-2019 (Grant # 307901/2019-0).

Institutional Review Board Statement: Not Applicable.

Informed Consent Statement: Not Applicable.

Data Availability Statement: Not Applicable.

Acknowledgments: This research used resources of the Central Multiusuário De Espectroscopia Do Nordeste (CEMENE), an open facility Brazilian spectroscopy laboratory network located at the Federal University of Pernambuco. The Severino Alves junior professor team staff is acknowledged for the assistance during the experiments. The authors would like to acknowledge the Center of Microscopy at the Universidade Federal de Minas Gerais (http://www.microscopia.ufmg.br) for providing the equipment and technical support for some experiments involving transmission electron microscopy.

Conflicts of Interest: The authors declare no conflict of intertest.

References

1. Zhang, X.; Shao, J.; Yan, C.; Qin, R.; Lu, Z.; Geng, H.; Xu, T.; Ju, L. A Review on Optoelectronic Device Applications of 2D Transition Metal Carbides and Nitrides. *Mater. Des.* **2021**, *200*, 109452. [CrossRef]
2. Bablich, A.; Kataria, S.; Lemme, M.C. Graphene and Two-Dimensional Materials for Optoelectronic Applications. *Electronics* **2016**, *5*, 13. [CrossRef]
3. Cai, Y.; Qin, A.; Tang, B.Z. Siloles in Optoelectronic Devices. *J. Mater. Chem. C* **2017**, *5*, 7375–7389. [CrossRef]
4. Prakash, J.; Samriti; Kumar, A.; Dai, H.; Janegitz, B.C.; Krishnan, V.; Swart, H.C.; Sun, S. Novel Rare Earth Metal–Doped One-Dimensional TiO_2 Nanostructures: Fundamentals and Multifunctional Applications. *Mater. Today Sustain.* **2021**, *13*, 100066. [CrossRef]
5. Vemuri, S.K.; Khanna, S.; Marathey, P.; Mukhopadhyay, I. Proceedings Titania Coated Zinc Oxide Nanorods: A Study of Structural and Optical Properties for Photocatalytic Applications. *Mater. Today Proc.* **2021**, *47*, 682–685. [CrossRef]
6. Muniyappan, S.; Solaiyammal, T.; Sudhakar, K.; Karthigeyan, A.; Murugakoothan, P. Conventional Hydrothermal Synthesis of Titanate Nanotubes: Systematic Discussions on Structural, Optical, Thermal and Morphological Properties. *Mod. Electron. Mater.* **2017**, *3*, 174–178. [CrossRef]
7. Badawi, A.; Althobaiti, M.G.; Ali, E.E.; Alharthi, S.S.; Alharbi, A.N. A Comparative Study of the Structural and Optical Properties of Transition Metals (M = Fe, Co, Mn, Ni) Doped ZnO Films Deposited by Spray-Pyrolysis Technique for Optoelectronic Applications. *Opt. Mater.* **2022**, *124*, 112055. [CrossRef]
8. Souza, H.T.S.; Oliveira, S.A.A.; Souza, J.S. Modulating the Photocatalytic Activity of Ag Nanoparticles-Titanate Nanotubes Heterojunctions through Control of Microwave-Assisted Synthesis Conditions. *J. Photochem. Photobiol. A Chem.* **2020**, *390*, 112264. [CrossRef]
9. Plodinec, M.; Gajović, A.; Jakša, G.; Žagar, K.; Čeh, M. High-Temperature Hydrogenation of Pure and Silver-Decorated Titanate Nanotubes to Increase Their Solar Absorbance for Photocatalytic Applications. *J. Alloy. Compd.* **2014**, *591*, 147–155. [CrossRef]
10. Buchholcz, B.; Varga, E.; Varga, T.; Plank, K.; Kiss, J.; Kónya, Z. Structure and Stability of Boron Doped Titanate Nanotubes and Nanowires. *Vacuum* **2017**, *138*, 120–124. [CrossRef]
11. Erjavec, B.; Kaplan, R.; Pintar, A. Effects of Heat and Peroxide Treatment on Photocatalytic Activity of Titanate Nanotubes. *Catal. Today* **2015**, *241*, 15–24. [CrossRef]
12. Vranješ, M.; Jakovljević, J.K.; Milošević, M.; Ćirić-Marjanović, G.; Stoiljković, M.; Konstantinović, Z.; Pavlović, V.; Milivojević, D.; Šaponjić, Z. Hydrothermal Synthesis of Mn2+ Doped Titanate Nanotubes: Investigation of Their Structure and Room Temperature Ferromagnetic Behavior. *Solid State Sci.* **2019**, *94*, 155–161. [CrossRef]
13. Kasuga, T.; Hiramatsu, M.; Hoson, A.; Sekino, T.; Niihara, K. Formation of Titanium Oxide Nanotube. *Langmuir* **1998**, *14*, 3160–3163. [CrossRef]
14. Gusmão, S.B.S.; Ghosh, A.; Marques, T.M.F.; Vieira, L.H.S.; Ferreira, O.P.; Silva-Filho, E.C.; Lobo, A.O.; Osajima, J.A.; Viana, B.C. Titanate-Based One-Dimensional Nano-Heterostructure: Study of Hydrothermal Reaction Parameters for Improved Photocatalytic Application. *Solid State Sci.* **2019**, *98*, 106043. [CrossRef]
15. Manique, M.C.; Silva, A.P.; Alves, A.K.; Bergmann, C.P. Titanate nanotubes produced from microwave-assisted hydrothermal synthesis: Characterization, adsorption and photocatalytic activity. *Braz. J. Chem. Eng.* **2017**, *34*, 331–339. [CrossRef]
16. Hafez, H.S.; Saif, M.; McLeskey, J.T., Jr.; Abdel-Mottaleb, M.S.A.; Yahia, I.S.; Story, T.; Knoff, W. Hydrothermal Preparation of Gd^{3+}- Doped Titanate Nanotubes: Magnetic Properties and Photovoltaic Performance. *Int. J. Photoenergy* **2009**, *2009*, 240402. [CrossRef]
17. Phan, T.D.; Vo, C.M.; Tran, T.M.T.; Luu, T.L.A.; Nguyen, X.S. Structural and Bandgap Properties of Titanium Dioxide Nanotube/Graphene Oxide Composites Prepared by a Facile Hydrothermal Method. *Mater. Res. Express* **2019**, *6*, 105054. [CrossRef]
18. Marques, T.M.F.; Luz-Lima, C.; Sacilloti, M.; Fujisawa, K.; Perea-Lopez, N.; Terrones, M.; Silva, E.N.; Ferreira, O.P.; Viana, B.C. Photoluminescence Enhancement of Titanate Nanotubes by Insertion of Rare Earth Ions in Their Interlayer Spaces. *J. Nanomater.* **2017**, *2017*, 3809807. [CrossRef]
19. Sales, D.A.; Marques, T.M.F.; Ghosh, A.; Gusmão, S.B.S.; Vasconcelos, T.L.; Luz-Lima, C.; Ferreira, O.P.; Hollanda, L.M.; Lima, I.S.; Silva-Filho, E.C.; et al. Synthesis of Silver-Cerium Titanate Nanotubes and Their Surface Properties and Antibacterial Applications. *Mater. Sci. Eng. C* **2020**, *115*, 111051. [CrossRef]

20. Gusmão, S.B.S.; Ghosh, A.; Marques, T.M.F.; Gusmão, G.O.M.; Oliveira, T.G.; Cavalcante, L.C.D.; Vasconcelos, T.L.; Abreu, G.J.P.; Guerra, Y.; Peña-Garcia, R.; et al. Structural and Magnetic Properties of Titanate Nano-Heterostructures Decorated with Iron Based Nanoparticles. *J. Phys. Chem. Solids* **2020**, *145*, 109561. [CrossRef]
21. Das, P.; Das, S.; Ratha, S.; Chakraborty, B.; Chatterjee, S. Ion Beam Engineered Hydrogen Titanate Nanotubes for Superior Energy Storage Application. *Electrochim. Acta* **2021**, *371*, 137774. [CrossRef]
22. Chen, L.; Ji, H.; Qi, J.; Huang, T.; Wang, C.; Liu, W. Degradation of Acetaminophen by Activated Peroxymonosulfate Using $Co(OH)_2$ Hollow Microsphere Supported Titanate Nanotubes: Insights into Sulfate Radical Production Pathway through $CoOH^+$ Activation. *Chem. Eng. J.* **2021**, *406*, 126877. [CrossRef]
23. Thi, D.; Thi, H.; Thi, D.; Thu, A.; Quang, P.; Hong, G. Schottky Contacts of (Au, Pt)/ Nanotube-Titanates for Fast Response to NO_2 Gas at Room Temperature. *Sens. Actuators B Chem.* **2017**, *244*, 941–948. [CrossRef]
24. Esteves, M.; Fernández-Werner, L.; Pignanelli, F.; Montenegro, B.; Belluzzi, M.; Pistón, M.; Chialanza, M.R.; Faccio, R.; Mombrú, Á.W. Synthesis, Characterization and Simulation of Lithium Titanate Nanotubes for Dye Sensitized Solar Cells. *Ceram. Int.* **2019**, *45*, 708–717. [CrossRef]
25. Yarali, M.; Biçer, E.; Gürsel, S.A.; Yürüm, A. Expansion of Titanate Nanotubes by the Use of a Surfactant and Its Improved Performance as an Anode in Li-Ion Batteries. *Electrochim. Acta* **2016**, *220*, 453–464. [CrossRef]
26. Freitas, T.S.; Marques, T.M.F.; Barros, L.N.L.C.; da Silva, J.H.; Cruz, R.P.; Pereira, R.L.S.; Silva, A.R.P.; Santos, A.T.L.; Ghosh, A.; Agressott, E.V.H.; et al. Synthesis of Cu-TiNT, Characterization, and Antibacterial Properties Evaluation. *Mater. Today Chem.* **2021**, *21*, 100539. [CrossRef]
27. Marques, T.M.F.; Ferreira, O.P.; Da Costa, J.A.P.; Fujisawa, K.; Terrones, M.; Viana, B.C. Study of the Growth of CeO_2 Nanoparticles onto Titanate Nanotubes. *J. Phys. Chem. Solids* **2015**, *87*, 213–220. [CrossRef]
28. Rónavári, A.; Kovács, D.; Vágvölgyi, C.; Kónya, Z.; Kiricsi, M.; Pfeiffer, I. Ion Exchange Defines the Biological Activity of Titanate Nanotubes. *J. Basic Microbiol.* **2016**, *56*, 557–565. [CrossRef]
29. Uematsu, E.; Itadani, A.; Uematsu, K.; Toda, K.; Sato, M. IR Study on Adsorption of Carbon Dioxide on Alkaline Earth Metal Ion-Exchanged Titanate Nanotubes at Room Temperature. *Vib. Spectrosc.* **2020**, *109*, 103088. [CrossRef]
30. Méndez-Galván, M.; Celaya, C.A.; Jaramillo-Quintero, O.A.; Muñiz, J.; Díaz, G.; Lara-García, H.A. Tuning the Band Gap of M-Doped Titanate Nanotubes (M = Fe, Co, Ni, and Cu): An Experimental and Theoretical Study. *Nanoscale Adv.* **2021**, *3*, 1382–1391. [CrossRef]
31. Dos Santos, N.M.; Rocha, J.M.; Matos, J.M.E.; Ferreira, O.P.; Filho, J.M.; Viana, B.C.; Oliveira, A.C. Metal Cations Intercalated Titanate Nanotubes as Catalysts for α,β Unsaturated Esters Production. *Appl. Catal. A Gen.* **2013**, *454*, 74–80. [CrossRef]
32. Li, M.; Zhao, J.; Li, Y.; Li, M.; Wu, Y.; Wang, C.; Jiao, H.; Na, P. Enhanced Adsorption of Cesium Ions by Electrochemically Switched Ion Exchange Method: Based on Surface-Synthetic $Na_2Ti_3O_7$ Nanotubes. *Colloids Surf. A Physicochem. Eng. Asp.* **2019**, *579*, 123712. [CrossRef]
33. Lopes, J.N.L.; Filho, J.C.S.; Messias, D.N.; Pilla, V.; Dantas, N.O.; Silva, A.C.A.; Andrade, A.A. Nd^{3+}-Doped TiO_2 Nanocrystals: Structural Changes, Excited-State Dynamics, and Luminescence Defects. *J. Lumin.* **2021**, *240*, 118461. [CrossRef]
34. Talane, T.E.; Mbule, P.S.; Noto, L.L.; Shingange, K.; Mhlongo, G.H.; Mothudi, B.M. Sol-Gel Preparation and Characterization of Er^{3+} Doped TiO_2 Luminescent Nanoparticles. *Mater. Res. Bull.* **2018**, *108*, 234–241. [CrossRef]
35. Conde-Gallardo, A.; Garcıía-Rocha, M.; Hernández-Calderón, I.; Palomino-Merino, R. Photoluminescence Properties of the Eu^{3+} Activator Ion in the TiO_2 Host Matrix. *Appl. Phys. Lett.* **2001**, *78*, 3436–3438. [CrossRef]
36. Jeon, S.; Braun, P. V Hydrothermal Synthesis of Er-Doped Luminescent TiO_2 Nanoparticles. *Chem. Mater.* **2003**, *15*, 1256–1263. [CrossRef]
37. Asahi, R.; Morikawa, T.; Ohwaki, T.; Aoki, K.; Taga, Y. Visible-Light Photocatalysis in Nitrogen-Doped Titanium Oxides. *Science* **2001**, *293*, 269–271. [CrossRef]
38. Chi, B.; Victorio, E.S.; Jin, T. Synthesis of Eu-Doped Photoluminescent Titania Nanotubes via a Two-Step Hydrothermal Treatment. *Nanotechnology* **2006**, *17*, 2234–2241. [CrossRef]
39. Radha, E.; Komaraiah, D.; Sayanna, R.; Sivakumar, J. Photoluminescence and Photocatalytic Activity of Rare Earth Ions Doped Anatase TiO_2 Thin Films. *J. Lumin.* **2022**, *244*, 118727. [CrossRef]
40. Komaraiah, D.; Radha, E.; James, J.; Kalarikkal, N.; Sivakumar, J.; Ramana Reddy, M.V.; Sayanna, R. Effect of Particle Size and Dopant Concentration on the Raman and the Photoluminescence Spectra of TiO_2:Eu^{3+} Nanophosphor Thin Films. *J. Lumin.* **2019**, *211*, 320–333. [CrossRef]
41. Chang, M.; Song, Y.; Sheng, Y.; Chen, J.; Guan, H.; Shi, Z.; Zhou, X.; Zheng, K.; Zou, H. Photoluminescence and Photocatalysis Properties of Dual-Functional Eu^{3+} -Doped Anatase Nanocrystals. *J. Phys. Chem. C* **2017**, *121*, 2369–2379. [CrossRef]
42. Meksi, M.; Turki, A.; Kochkar, H.; Bousselmi, L.; Guillard, C.; Berhault, G. The Role of Lanthanum in the Enhancement of Photocatalytic Properties of TiO_2 Nanomaterials Obtained by Calcination of Hydrogenotitanate Nanotubes. *Appl. Catal. B Environ.* **2016**, *181*, 651–660. [CrossRef]
43. Obregón, S.; Colón, G. Evidence of Upconversion Luminescence Contribution to the Improved Photoactivity of Erbium Doped TiO_2 Systems. *Chem. Commun.* **2012**, *48*, 7865. [CrossRef] [PubMed]
44. Castañeda-Contreras, J.; Marañón-Ruiz, V.F.; Chiu-Zárate, R.; Pérez-Ladrón de Guevara, H.; Rodriguez, R.; Michel-Uribe, C. Photocatalytic Activity of Erbium-Doped TiO_2 Nanoparticles Immobilized in Macro-Porous Silica Films. *Mater. Res. Bull.* **2012**, *47*, 290–295. [CrossRef]

45. Pérez, J.A.B.; Courel, M.; Valderrama, R.C.; Hernández, I.; Pal, M.; Delgado, F.P.; Mathews, N.R. Structural, Optical, and Photoluminescence Properties of Erbium Doped TiO_2 Films. *Vacuum* **2019**, *169*, 108873. [CrossRef]
46. Cho, H.; Joo, H.; Kim, H.; Kim, J.-E.; Kang, K.-S.; Yoon, J. Enhanced Photocatalytic Activity of TiO_2 Nanotubes Decorated with Erbium and Reduced Graphene Oxide. *Appl. Surf. Sci.* **2021**, *565*, 150459. [CrossRef]
47. Singh, K.; Harish, S.; Kristy, A.P.; Shivani, V.; Archana, J.; Navaneethan, M.; Shimomura, M.; Hayakawa, Y. Erbium Doped TiO_2 Interconnected Mesoporous Spheres as an Efficient Visible Light Catalyst for Photocatalytic Applications. *Appl. Surf. Sci.* **2018**, *449*, 755–763. [CrossRef]
48. Dhanalakshmi, J.; Selvakumari, C. Improved Photo-Induced Charge Carriers Separation through the Addition of Erbium on TiO_2 Nanoparticles and Its Effect on Photocatalytic Degradation of Rhodamine B. *Spectrochim. Acta Part A Mol. Biomol. Spectrosc.* **2018**, *190*, 524–533. [CrossRef]
49. Cho, H.; Joo, H.; Kim, H.; Kim, J.-E.; Kang, K.-S.; Yoon, J. Improved Photoelectrochemical Properties of TiO_2 Nanotubes Doped with Er and Effects on Hydrogen Production from Water Splitting. *Chemosphere* **2021**, *267*, 129289. [CrossRef]
50. Mazierski, P.; Mikolajczyk, A.; Bajorowicz, B.; Malankowska, A.; Zaleska-Medynska, A.; Nadolna, J. The Role of Lanthanides in TiO_2-Based Photocatalysis: A Review. *Appl. Catal. B Environ.* **2018**, *233*, 301–317. [CrossRef]
51. Kiatkittipong, K.; Scott, J.; Amal, R. Hydrothermally Synthesized Titanate Nanostructures: Impact of Heat Treatment on Particle Characteristics and Photocatalytic Properties. *ACS Appl. Mater. Interfaces* **2011**, *3*, 3988–3996. [CrossRef]
52. Akbari, M.; Mirzaei, A.A.; Arsalanfar, M. Microemulsion Based Synthesis of Promoted Fe–Co/MgO Nanocatalyst: Influence of Calcination Atmosphere on the Physicochemical Properties, Activity and Light Olefins Selectivity for Hydrogenation of Carbon Monoxide. *Mater. Chem. Phys.* **2020**, *249*, 123003. [CrossRef]
53. Wu, M.; Zhang, M.; Lv, T.; Guo, M.; Li, J.; Okonkwo, C.A.; Liu, Q.; Jia, L. The Effect of Calcination Atmosphere upon the Photocatalytic Performance of Au-La_2O_3/TiO_2 for Hydrogen Production from Formic Acid. *Appl. Catal. A Gen.* **2017**, *547*, 96–104. [CrossRef]
54. Slimen, H.; Lachheb, H.; Qourzal, S.; Assabbane, A.; Houas, A. The Effect of Calcination Atmosphere on the Structure and Photoactivity of TiO_2 Synthesized through an Unconventional Doping Using Activated Carbon. *J. Environ. Chem. Eng.* **2015**, *3*, 922–929. [CrossRef]
55. Galetti, A.E.; Gomez, M.F.; Arrua, L.A.; Abello, M.C. Ethanol Steam Reforming over Ni/$ZnAl_2O_4$-CeO_2. Influence of Calcination Atmosphere and Nature of Catalytic Precursor. *Appl. Catal. A Gen.* **2011**, *408*, 78–86. [CrossRef]
56. Blasco-Tamarit, E.; Solsona, B.; Sánchez-Tovar, R.; García-García, D.; Fernández-Domene, R.M.; García-Antón, J. Influence of Annealing Atmosphere on Photoelectrochemical Response of TiO_2 Nanotubes Anodized under Controlled Hydrodynamic Conditions. *J. Electroanal. Chem.* **2021**, *897*, 115579. [CrossRef]
57. Rodrigues, G.L.C.; de Oliveira, T.G.; Gusmão, S.B.S.; Marques, T.M.F.; Ferreira, O.P.; Ghosh, A.; dos Santos, C.C.; Milani, R.; Garcia, R.R.P.; Viana, B.C. Titanate Nanotubes: Effect of Rare Earth Insertion, Thermal Treatment and Their Optical Properties. *Opt. Mater.* **2022**, *127*, 112302. [CrossRef]
58. Gusmão, S.B.S.; Ghosh, A.; Marques, T.M.F.; Ferreira, O.P.; Lobo, A.O.; Osajima, J.A.O.; Luz-Lima, C.; Sousa, R.R.M.; Matos, J.M.E.; Viana, B.C. One-Pot Synthesis of Titanate Nanotubes Decorated with Anatase Nanoparticles Using a Microwave-Assisted Hydrothermal Reaction. *J. Nanomater.* **2019**, *2019*, 4825432. [CrossRef]
59. Jose, M.; Szymańska, K.; Szymański, K.; Moszyński, D.; Mozia, S. Effect of Copper Salts on the Characteristics and Antibacterial Activity of Cu-Modified Titanate Nanotubes. *J. Environ. Chem. Eng.* **2020**, *8*, 104550. [CrossRef]
60. Cech, O.; Castkova, K.; Chladil, L.; Dohnal, P.; Cudek, P.; Libich, J.; Vanysek, P. Synthesis and Characterization of $Na_2Ti_6O_{13}$ and $Na_2Ti_6O_{13}$/$Na_2Ti_3O_7$ Sodium Titanates with Nanorod-like Structure as Negative Electrode Materials for Sodium-Ion Batteries. *J. Energy Storage* **2017**, *14*, 391–398. [CrossRef]
61. Gajović, A.; Friščić, I.; Plodinec, M.; Iveković, D. High Temperature Raman Spectroscopy of Titanate Nanotubes. *J. Mol. Struct.* **2009**, *924–926*, 183–191. [CrossRef]
62. Zárate, R.A.; Fuentes, S.; Cabrera, A.L.; Fuenzalida, V.M. Structural Characterization of Single Crystals of Sodium Titanate Nanowires Prepared by Hydrothermal Process. *J. Cryst. Growth* **2008**, *310*, 3630–3637. [CrossRef]
63. Zhu, K.R.; Yuan, Y.; Zhang, M.S.; Hong, J.M.; Deng, Y.; Yin, Z. Structural Transformation from $NaHTi_3O_7$ Nanotube to $Na_2Ti_6O_{13}$ Nanorod. *Solid State Commun.* **2007**, *144*, 450–453. [CrossRef]
64. Rónavári, A.; Buchholcz, B.; Kukovecz, Á.; Kónya, Z. Structure and Stability of Pristine and Bi and/or Sb Decorated Titanate Nanotubes. *J. Mol. Struct.* **2013**, *1044*, 104–108. [CrossRef]
65. Ferreira, O.P.; Souza Filho, A.G.; Mendes Filho, J.; Alves, O.L. Unveiling the Structure and Composition of Titanium Oxide Nanotubes through Ion Exchange Chemical Reactions and Thermal Decomposition Processes. *J. Braz. Chem. Soc.* **2006**, *17*, 393–402. [CrossRef]
66. Marques, T.M.F.; Morais, R.N.; Nobre, F.X.; Rocha, J.M.; Ghosh, A.; Soares, T.A.S.; Viana, B.C.; Machado, G.; Costa, J.C.S.; De Matos, J.M.E. Hydrogen Production from Aqueous Glycerol Using Titanate Nanotubes Decorated with Au Nanoparticles as Photocatalysts. *An. Acad. Bras. Ciências* **2019**, *91*, 1–15. [CrossRef]
67. Marques, T.M.F.; Strayer, M.E.; Ghosh, A.; Silva, A.; Ferreira, O.P.; Fujisawa, K.; Alves da Cunha, J.R.; Abreu, G.J.P.; Terrones, M.; Mallouk, T.E.; et al. Homogeneously Dispersed CeO_2 Nanoparticles on Exfoliated Hexaniobate Nanosheets. *J. Phys. Chem. Solids* **2017**, *111*, 335–342. [CrossRef]

68. Xiao, N.; Li, Z.; Liu, J.; Gao, Y. Effects of Calcination Temperature on the Morphology, Structure and Photocatalytic Activity of Titanate Nanotube Thin Films. *Thin Solid Film.* **2010**, *519*, 541–548. [CrossRef]
69. Wang, S.; Shi, H.; Xia, Y.; Liang, S.; Pei, M.; Xu, Z.; Pei, X.; Hu, Y.; Wu, X. Electrospun-Based Nanofibers for Sodium and Potassium Ion Storage: Structure Design for Alkali Metal Ions with Large Radius. *J. Alloy. Compd.* **2022**, *918*, 165680. [CrossRef]
70. Junaid, M.; Kousar, I.; Gulbadan, S.; Khan, M.A.; Yousuf, M.A.; Baig, M.M.; Ashraf, G.A.; Somaily, H.H.; Morsi, M. Structural, Microstructural, Spectral, and Dielectric Properties of Erbium Substituted Spinel Ferrites. *Phys. B Condens. Matter* **2022**, *641*, 414120. [CrossRef]
71. Ali, I.O.; Salama, T.M.; El-Gawad, A.A.; El-Henawy, A.A.; Ghazy, M.B.; Bakr, M.F. Silver Nanoparticles @ Titanate Nanotubes Composite: Synthesis, Characterization, Applications and Docking. *Inorg. Chem. Commun.* **2022**, *137*, 109187. [CrossRef]
72. Viana, B.C.; Ferreira, O.P.; Souza Filho, A.G.; Mendes Filho, J.; Alves, O.L. Structural, Morphological and Vibrational Properties of Titanate Nanotubes and Nanoribbons. *J. Braz. Chem. Soc.* **2009**, *20*, 167–175. [CrossRef]
73. Marques, T.M.F.; Sales, D.A.; Silva, L.S.; Bezerra, R.D.S.; Silva, M.S.; Osajima, J.A.; Ferreira, O.P.; Ghosh, A.; Silva Filho, E.C.; Viana, B.C.; et al. Amino-Functionalized Titanate Nanotubes for Highly Efficient Removal of Anionic Dye from Aqueous Solution. *Appl. Surf. Sci.* **2020**, *512*, 145659. [CrossRef]
74. Viana, B.C.; Ferreira, O.P.; Filho, A.G.S.; Hidalgo, A.A.; Filho, J.M.; Alves, O.L. Alkali Metal Intercalated Titanate Nanotubes: A Vibrational Spectroscopy Study. *Vib. Spectrosc.* **2011**, *55*, 183–187. [CrossRef]
75. Manfroi, D.C.; dos Anjos, A.; Cavalheiro, A.A.; Perazolli, L.A.; Varela, J.A.; Zaghete, M.A. Titanate Nanotubes Produced from Microwave-Assisted Hydrothermal Synthesis: Photocatalytic and Structural Properties. *Ceram. Int.* **2014**, *40*, 14483–14491. [CrossRef]
76. Li, P.; Wang, P.; Qian, S.; Yu, H.; Lin, X.; Shui, M.; Zheng, X.; Long, N.; Shu, J. Synthesis of $Na_2Ti_6O_{13}$ Nanorods as Possible Anode Materials for Rechargeable Lithium Ion Batteries. *Electrochim. Acta* **2016**, *187*, 46–54. [CrossRef]
77. Liang, J.; Wang, J.; Song, K.; Wang, X.; Yu, K.; Liang, C. Enhanced Photocatalytic Activities of Nd-Doped TiO_2 under Visible Light Using a Facile Sol-Gel Method. *J. Rare Earths* **2020**, *38*, 148–156. [CrossRef]
78. Chakraborty, A.K.; Qi, Z.; Chai, S.Y.; Lee, C.; Park, S.-Y.; Jang, D.-J.; Lee, W.I. Formation of Highly Crystallized TiO_2(B) and Its Photocatalytic Behavior. *Appl. Catal. B Environ.* **2010**, *93*, 368–375. [CrossRef]
79. Kobwittaya, K.; Oishi, Y.; Torikai, T.; Yada, M.; Watari, T.; Luitel, H.N. Bright Red Upconversion Luminescence from Er^{3+} and Yb^{3+} Co-Doped ZnO-TiO_2 Composite Phosphor Powder. *Ceram. Int.* **2017**, *43*, 13505–13515. [CrossRef]
80. Lin, C.; Chao, J.; Liu, C.; Chang, J.; Wang, F. Effect of Calcination Temperature on the Structure of a Pt/TiO_2 (B) Nanofiber and Its Photocatalytic Activity in Generating H 2. *Langmuir* **2008**, *24*, 9907–9915. [CrossRef]
81. Sreekantan, S.; Wei, L.C. Study on the Formation and Photocatalytic Activity of Titanate Nanotubes Synthesized via Hydrothermal Method. *J. Alloy. Compd.* **2010**, *490*, 436–442. [CrossRef]
82. de Carvalho, D.C.; Oliveira, A.C.; Ferreira, O.P.; Filho, J.M.; Tehuacanero-Cuapa, S.; Oliveira, A.C. Titanate Nanotubes as Acid Catalysts for Acetalization of Glycerol with Acetone: Influence of the Synthesis Time and the Role of Structure on the Catalytic Performance. *Chem. Eng. J.* **2017**, *313*, 1454–1467. [CrossRef]
83. Anbharasi, L.; Bhanu Rekha, E.A.; Rahul, V.R.; Roy, B.; Gunaseelan, M.; Yamini, S.; Adusumalli, V.N.K.B.; Sarkar, D.; Mahalingam, V.; Senthilselvan, J. Tunable Emission and Optical Trapping of Upconverting LiYF4:Yb,Er Nanocrystal. *Opt. Laser Technol.* **2020**, *126*, 106109. [CrossRef]
84. Reszczyńska, J.; Grzyb, T.; Sobczak, J.W.; Lisowski, W.; Gazda, M.; Ohtani, B.; Zaleska, A. Visible Light Activity of Rare Earth Metal Doped (Er^{3+}, Yb^{3+} or Er^{3+}/Yb^{3+}) Titania Photocatalysts. *Appl. Catal. B Environ.* **2015**, *163*, 40–49. [CrossRef]
85. Yang, Y.; Zhang, C.; Xu, Y.; Wang, H.; Li, X.; Wang, C. Electrospun Er:TiO_2 Nanofibrous Films as Efficient Photocatalysts under Solar Simulated Light. *Mater. Lett.* **2010**, *64*, 147–150. [CrossRef]
86. Kim, M.; Hwang, S.-H.; Lim, S.K.; Kim, S. Effects of Ion Exchange and Calcinations on the Structure and Photocatalytic Activity of Hydrothermally Prepared Titanate Nanotubes. *Cryst. Res. Technol.* **2012**, *47*, 1190–1194. [CrossRef]
87. Turki, A.; Kochkar, H.; Guillard, C.; Berhault, G.; Ghorbel, A. Effect of Na Content and Thermal Treatment of Titanate Nanotubes on the Photocatalytic Degradation of Formic Acid. *Appl. Catal. B Environ.* **2013**, *138–139*, 401–415. [CrossRef]
88. Rodríguez-González, V.; Obregón-Alfaro, S.; Lozano-Sánchez, L.M.; Lee, S.-W. Rapid Microwave-Assisted Synthesis of One-Dimensional Silver–H2Ti3O7 Nanotubes. *J. Mol. Catal. A Chem.* **2012**, *353–354*, 163–170. [CrossRef]
89. Loan, T.T.; Huong, V.H.; Huyen, N.T.; Van Quyet, L.; Bang, N.A.; Long, N.N. Anatase to Rutile Phase Transformation of Iron-Doped Titanium Dioxide Nanoparticles: The Role of Iron Content. *Opt. Mater.* **2021**, *111*, 110651. [CrossRef]
90. Park, H.; Goto, T.; Cho, S.; Nishida, H.; Sekino, T. Enhancing Visible Light Absorption of Yellow-Colored Peroxo-Titanate Nanotubes Prepared Using Peroxo Titanium Complex Ions. *ACS Omega* **2020**, *5*, 21753–21761. [CrossRef]
91. Barbieriková, Z.; Lončarević, D.; Papan, J.; Vukoje, I.D.; Stoiljković, M.; Phillip Ahrenkiel, S.; Nedeljković, J.M. Photocatalytic Hydrogen Evolution over Surface-Modified Titanate Nanotubes by 5-Aminosalicylic Acid Decorated with Silver Nanoparticles. *Adv. Powder Technol.* **2020**, *31*, 4683–4690. [CrossRef]
92. Gao, T.; Wu, Q.; Fjellvåg, H.; Norby, P. Topological Properties of Titanate Nanotubes. *J. Phys. Chem. C* **2008**, *112*, 8548–8552. [CrossRef]
93. Bem, V.; Neves, M.C.; Nunes, M.R.; Silvestre, A.J.; Monteiro, O.C. Influence of the Sodium/Proton Replacement on the Structural, Morphological and Photocatalytic Properties of Titanate Nanotubes. *J. Photochem. Photobiol. A Chem.* **2012**, *232*, 50–56. [CrossRef]
94. Wang, C.; Chou, C. The Effects of Sodium Content and Hydrogenation of TiO_2 Nanotubes on Photocatalytic Activity. *J. Photochem. Photobiol. A Chem.* **2018**, *358*, 226–235. [CrossRef]

95. Peng, Y.-P.; Lo, S.-L.; Ou, H.-H.; Lai, S.-W. Microwave-Assisted Hydrothermal Synthesis of N-Doped Titanate Nanotubes for Visible-Light-Responsive Photocatalysis. *J. Hazard. Mater.* **2010**, *183*, 754–758. [CrossRef]
96. Zhang, L.; Lin, H.; Wang, N.; Lin, C.; Li, J. The Evolution of Morphology and Crystal Form of Titanate Nanotubes under Calcination and Its Mechanism. *J. Alloy. Compd.* **2007**, *431*, 230–235. [CrossRef]
97. Liu, Z.; Zhang, Q.; Qin, L. Reduction in the Electronic Band Gap of Titanium Oxide Nanotubes. *Solid State Commun.* **2007**, *141*, 168–171. [CrossRef]
98. Kukovecz, Á.; Kordás, K.; Kiss, J.; Kónya, Z. Atomic Scale Characterization and Surface Chemistry of Metal Modified Titanate Nanotubes and Nanowires. *Surf. Sci. Rep.* **2016**, *71*, 473–546. [CrossRef]
99. Qamar, M.; Yoon, C.R.; Oh, H.J.; Kim, D.H.; Jho, J.H.; Lee, K.S.; Lee, W.J.; Lee, H.G.; Kim, S.J. Effect of Post Treatments on the Structure and Thermal Stability of Titanate Nanotubes. *Nanotechnology* **2006**, *17*, 5922–5929. [CrossRef]
100. Akshay, V.R.; Arun, B.; Mandal, G.; Vasundhara, M. Visible Range Optical Absorption, Urbach Energy Estimation and Paramagnetic Response in Cr-Doped TiO_2 Nanocrystals Derived by a Sol–Gel Method. *Phys. Chem. Chem. Phys.* **2019**, *21*, 12991–13004. [CrossRef]
101. Bokare, A.; Pai, M.; Athawale, A.A. Surface Modified Nd Doped TiO_2 Nanoparticles as Photocatalysts in UV and Solar Light Irradiation. *Sol. Energy* **2013**, *91*, 111–119. [CrossRef]
102. Liqiang, J.; Yichun, Q.; Baiqi, W.; Shudan, L.; Baojiang, J.; Libin, Y.; Wei, F.; Honggang, F.; Jiazhong, S. Review of Photoluminescence Performance of Nano-Sized Semiconductor Materials and Its Relationships with Photocatalytic Activity. *Sol. Energy Mater. Sol. Cells* **2006**, *90*, 1773–1787. [CrossRef]
103. Tang, Q.; Sun, Z.; Wang, P.; Li, Q.; Wang, H.; Wu, Z. Enhanced CO_2 Photocatalytic Reduction Performance on Alkali and Alkaline Earth Metal Ion-Exchanged Hydrogen Titanate Nanotubes. *Appl. Surf. Sci.* **2019**, *463*, 456–462. [CrossRef]
104. Pal, M.; Pal, U.; Jiménez, J.M.G.Y.; Pérez-Rodríguez, F. Effects of Crystallization and Dopant Concentration on the Emission Behavior of TiO_2:Eu Nanophosphors. *Nanoscale Res. Lett.* **2012**, *7*, 1. [CrossRef]
105. Reszczyńska, J.; Grzyb, T.; Wei, Z.; Klein, M.; Kowalska, E.; Ohtani, B.; Zaleska-Medynska, A. Photocatalytic Activity and Luminescence Properties of RE^{3+}-TiO_2 Nanocrystals Prepared by Sol-Gel and Hydrothermal Methods. *Appl. Catal. B Environ.* **2016**, *181*, 825–837. [CrossRef]
106. Barrocas, B.; Conceição Oliveira, M.; Nogueira, H.I.S.; Fateixa, S.; Monteiro, O.C. A Comparative Study on Emergent Pollutants Photo-Assisted Degradation Using Ruthenium Modified Titanate Nanotubes and Nanowires as Catalysts. *J. Environ. Sci.* **2020**, *92*, 38–51. [CrossRef] [PubMed]
107. Zhang, J.; Xu, L.J.; Zhu, Z.Q.; Liu, Q.J. Synthesis and Properties of (Yb, N)-TiO_2 Photocatalyst for Degradation of Methylene Blue (MB) under Visible Light Irradiation. *Mater. Res. Bull.* **2015**, *70*, 358–364. [CrossRef]
108. Bandi, V.R.; Raghavan, C.M.; Grandhe, B.K.; Kim, S.S.; Jang, K.; Shin, D.-S.; Yi, S.-S.; Jeong, J.-H. Synthesis, Structural and Optical Properties of Pure and Rare-Earth Ion Doped TiO_2 Nanowire Arrays by a Facile Hydrothermal Technique. *Thin Solid Film.* **2013**, *547*, 207–211. [CrossRef]
109. Liqiang, J.; Xiaojun, S.; Baifu, X.; Baiqi, W.; Weimin, C.; Honggang, F. The Preparation and Characterization of La Doped TiO_2 Nanoparticles and Their Photocatalytic Activity. *J. Solid State Chem.* **2004**, *177*, 3375–3382. [CrossRef]
110. Kim, H.R.; Lee, T.G.; Shul, Y.-G. Photoluminescence of La/Ti Mixed Oxides Prepared Using Sol–Gel Process and Their PCBA Photodecomposition. *J. Photochem. Photobiol. A Chem.* **2007**, *185*, 156–160. [CrossRef]
111. Yildirim, S.; Yurddaskal, M.; Dikici, T.; Aritman, I.; Ertekin, K.; Celik, E. Structural and Luminescence Properties of Undoped, Nd^{3+} and Er^{3+} Doped TiO_2 Nanoparticles Synthesized by Flame Spray Pyrolysis Method. *Ceram. Int.* **2016**, *42*, 10579–10586. [CrossRef]
112. Zhao, J.-G.; Zhang, W.-Y.; Ma, Z.-W.; Xie, E.-Q.; Zhao, A.-K.; Liu, Z.-J. Structure and Photoluminescence Properties of Er^{3+} -Doped TiO_2 -SiO_2 Powders Prepared by Sol—Gel Method. *Chin. Phys. B* **2011**, *20*, 87701. [CrossRef]
113. Komaraiah, D.; Radha, E.; Kalarikkal, N.; Sivakumar, J.; Ramana Reddy, M.V.; Sayanna, R. Structural, Optical and Photoluminescence Studies of Sol-Gel Synthesized Pure and Iron Doped TiO_2 Photocatalysts. *Ceram. Int.* **2019**, *45*, 25060–25068. [CrossRef]
114. Amy, L.; Favre, S.; Gau, D.L.; Faccio, R. The Effect of Morphology on the Optical and Electrical Properties of Sodium Titanate Nanostructures. *Appl. Surf. Sci.* **2021**, *555*, 149610. [CrossRef]
115. Montoncello, F.; Carotta, M.C.; Cavicchi, B.; Ferroni, M.; Giberti, A.; Guidi, V.; Malagù, C.; Martinelli, G.; Meinardi, F. Near-Infrared Photoluminescence in Titania: Evidence for Phonon-Replica Effect. *J. Appl. Phys.* **2003**, *94*, 1501–1505. [CrossRef]
116. Fang, D.; Huang, K.; Liu, S.; Huang, J. Fabrication and Photoluminiscent Properties of Titanium Oxide Nanotube Arrays. *J. Braz. Chem. Soc.* **2008**, *19*, 1059–1064. [CrossRef]
117. Viana, B.C.; Ferreira, O.P.; Souza Filho, A.G.; Rodrigues, C.M.; Moraes, S.G.; Mendes Filho, J.; Alves, O.L. Decorating Titanate Nanotubes with CeO_2 Nanoparticles. *J. Phys. Chem. C* **2009**, *113*, 20234–20239. [CrossRef]
118. Liu, Z.; Li, X.; Mayyas, M.; Koshy, P.; Hart, J.N.; Sorrell, C.C. Planar-Dependent Oxygen Vacancy Concentrations in Photocatalytic CeO_2 Nanoparticles. *CrystEngComm* **2018**, *20*, 204–212. [CrossRef]
119. Younis, A.; Chu, D.; Kaneti, Y.V.; Li, S. Tuning the Surface Oxygen Concentration of {111} Surrounded Ceria Nanocrystals for Enhanced Photocatalytic Activities. *Nanoscale* **2016**, *8*, 378–387. [CrossRef]

Disclaimer/Publisher's Note: The statements, opinions and data contained in all publications are solely those of the individual author(s) and contributor(s) and not of MDPI and/or the editor(s). MDPI and/or the editor(s) disclaim responsibility for any injury to people or property resulting from any ideas, methods, instructions or products referred to in the content.